Supplementary Information for "Multisite exchange paths and zigzag antiferromagnetism in the Kitaev material RuI_3 monolayer"

Ke Yang,[1,2] Zhefu Wu,[2] Yaozhenghang Ma,[2] Feng-Ren Fan,[2,3] Yuxuan Zhou,[2] and Hua Wu[2,4,5,*]

[1] *School of Physics, Faculty of Basic Sciences, University of Shanghai for Science and Technology, Shanghai 200093, China*
[2] *Laboratory for Computational Physical Sciences (MOE), State Key Laboratory of Surface Physics, and Department of Physics, Fudan University, Shanghai 200433, China*
[3] *Institute for Quantum Science, School of Physical Science and Technology, Soochow University, Suzhou 215006, China*
[4] *Shanghai Qi Zhi Institute, Shanghai 200232, China*
[5] *Hefei National Laboratory, Hefei 230088, China*

CONTENTS

I. Crystal and electronic structure 1
II. Low-spin state of Ru^{3+} 2
III. Wannier functions 3
IV. Single-ion Hamiltonian and the $J_{\rm eff} = 1/2$ doublet 4
V. Hopping channels 6
VI. Two-site ED and the pseudospin projection 7
VII. Finite clusters and the extraction of the exchange couplings 8
VIII. Dependence of the six-site couplings on U, J_H and λ 15
IX. Magnetic ground state and phase diagram 15
X. Density-matrix renormalization group 20
XI. Linear spin-wave theory 23
XII. Monte Carlo simulations 24
References 26

I. Crystal and electronic structure

Monolayer RuI_3 is a honeycomb layer of edge-sharing RuI_6 octahedra, with the three Kitaev bonds X, Y and Z and their Kitaev axes shown in Fig. 1 of the main text. The RuI_6 octahedron is trigonally distorted along the [111] axis, which lowers the site symmetry from $O_{\rm h}$ to D_3. The Ru site has no inversion center, because the inversion centers of the layer lie at the midpoints of the nearest-neighbor (1NN) bonds. Throughout, $\delta < 0$ denotes compression and $\delta > 0$ elongation, and $\delta_{\rm tri} = 3|\delta|$ is the resulting splitting between the a_{1g} and e_g^π orbitals.

Figure S1 shows the nonmagnetic band structure and density of states (DOS) of RuI_3 from density functional theory (DFT) in the GGA. The Ru t_{2g} manifold lies at the Fermi level E_F and is strongly hybridized with the I $5p$ states. It is separated from the e_g manifold by $\Delta_{\rm cf} \approx 2$ eV. This splitting agrees with the crystal-field parameter $10Dq = 2.05$ eV from the multiplet analysis of Ru L_3-edge resonant inelastic x-ray scattering [1]. RuI_3 is metallic at the GGA level, whereas the earlier DFT+U calculations find the monolayer insulating [2].

* wuh@fudan.edu.cn

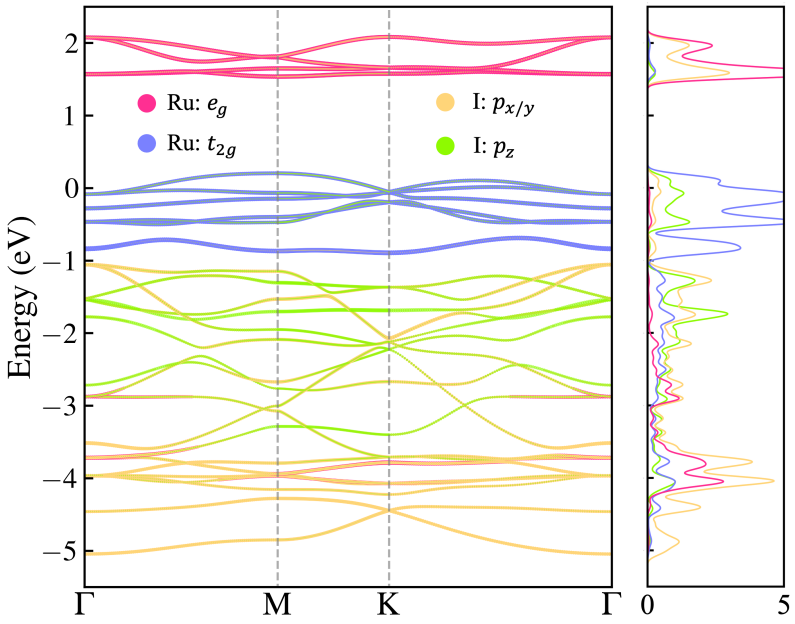

Figure S1. Nonmagnetic generalized-gradient approximation (GGA) band structure and density of states (DOS) of RuI_3, colored by orbital character: Ru e_g (red), Ru t_{2g} (blue), I $p_{x/y}$ (gold) and I p_z (green). For each iodine, p_z is the $5p$ orbital along the cubic axis γ of the Ru–Ru bond that it bridges and mediates t_2. The other two $5p$ orbitals are $p_{x/y}$.

II. Low-spin state of Ru^{3+}

The high-spin $t_{2g}^3 e_g^2$ ($S = 5/2$) and low-spin t_{2g}^5 ($S = 1/2$) configurations are illustrated in Fig. S2. Promoting two electrons from t_{2g} to e_g requires $2\Delta_{\rm cf}$ in crystal field energy, against which the high-spin configuration gains Hund exchange energy.

We count the Hund exchange as $-J_H$ per pair of parallel spins. The high-spin configuration with its $\binom{5}{2} = 10$ parallel pairs then has $E_{\rm HS} = 2\Delta_{\rm cf} - 10J_H$, and the low-spin configuration with four parallel pairs (three among the spin-up and one among the spin-down electrons) has $E_{\rm LS} = -4J_H$. This configuration-energy estimate gives $E_{\rm HS} - E_{\rm LS} = 2\Delta_{\rm cf} - 6J_H$. The Coulomb repulsion of the ten electron pairs is common to both configurations and omitted. Spin-flip and pair-hopping terms and the multiplet mixing by the spin-orbit coupling (SOC) are not included in this estimate, so $\Delta_{\rm cf} = 3J_H$ is not an exact multiplet boundary.

The adopted $J_H = 0.3$ eV gives $3J_H = 0.9$ eV, well below $\Delta_{\rm cf} \approx 2$ eV. The resulting energy difference of approximately 2 eV favors the low-spin configuration. Its single t_{2g} hole carries $S = 1/2$ and effective orbital angular momentum $L_{\rm eff} = 1$, providing the local degrees of freedom of the pseudospin model.

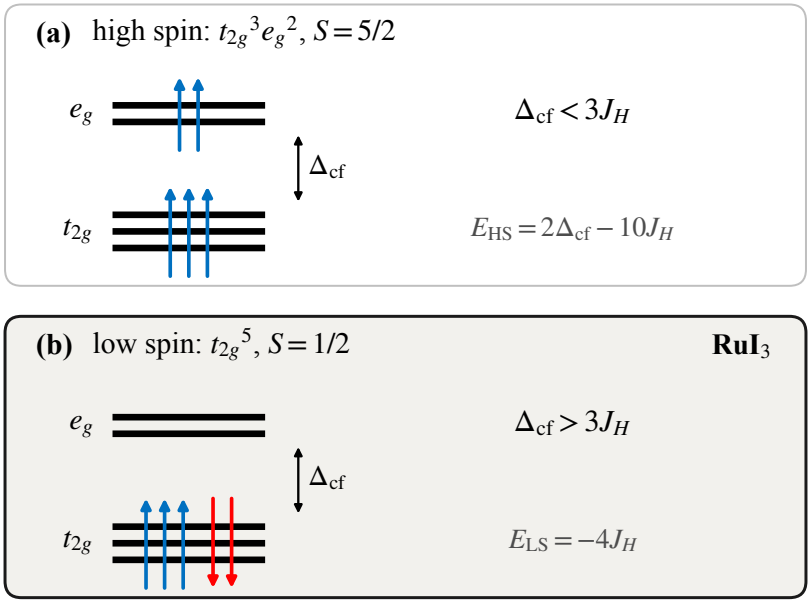

Figure S2. High- and low-spin configurations of the Ru^{3+} ($4d^5$) ion: (a) $t_{2g}^3 e_g^2$ ($S = 5/2$) and (b) t_{2g}^5 ($S = 1/2$). Blue and red arrows denote spin-up and spin-down electrons. The energies count only the Hund exchange, $-J_H$ per pair of parallel spins.

III. Wannier functions

We construct the Wannier functions of the three Ru t_{2g} orbitals with WANNIER90 [3] from the nonmagnetic GGA bands without SOC. The six t_{2g} bands are disentangled from the I $5p$ and Ru e_g bands within an energy window that contains them, and the disentangled subspace is projected onto the Ru t_{2g} orbitals. The subsequent spread minimization is not performed, so that each Wannier function keeps its t_{2g} symmetry. This symmetry is required for the orbital-resolved hopping channels of Sec. V. The Wannier-interpolated bands reproduce the DFT t_{2g} bands [Fig. S3(a)]. The resulting d_{xy}, d_{yz} and d_{xz} Wannier functions [Figs. S3(b)–(d)] are centered on the Ru sites but have significant weight on the surrounding ligand I sites owing to the strong Ru $4d$–I $5p$ hybridization.

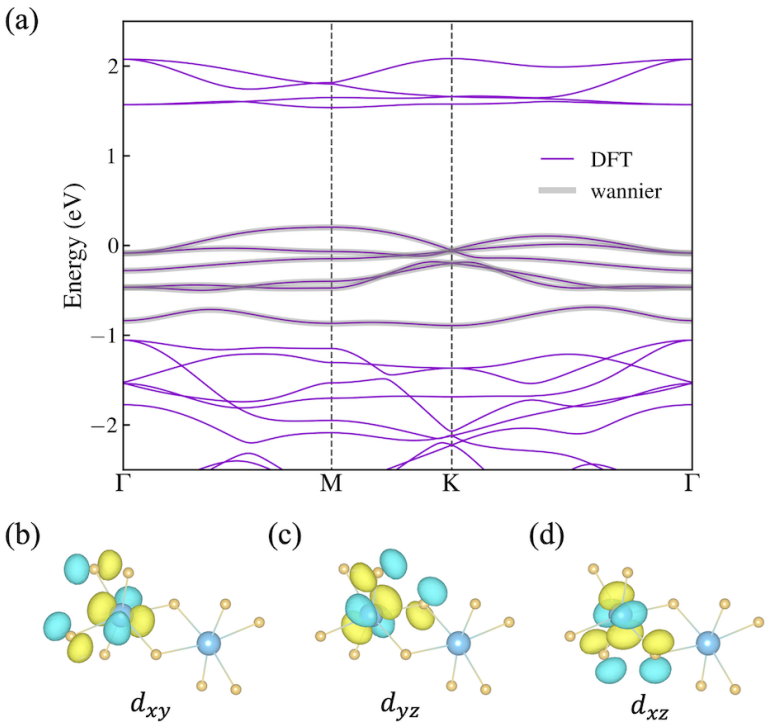

Figure S3. (a) DFT bands (magenta) and Wannier-interpolated t_{2g} bands (gray) of RuI_3. (b)–(d) The t_{2g} Wannier functions d_{xy}, d_{yz} and d_{xz}.

IV. Single-ion Hamiltonian and the $J_{\rm eff} = 1/2$ doublet

The single-ion Hamiltonian $H_{\rm one} = H_{\rm CF} + H_U + H_{\rm SOC}$ [Eq. (1) of the main text] is constructed in the t_{2g} basis (d_{xz}, d_{yz}, d_{xy}). The Wannier calculation gives the on-site crystal field matrix [Eq. (2) of the main text] as (in meV)

$$H_{\rm CF} = \begin{pmatrix} -1472.1 & -14.7 & -14.7 \\ -14.7 & -1472.1 & -14.7 \\ -14.7 & -14.7 & -1472.1 \end{pmatrix}. \tag{S1}$$

The uniform diagonal offset does not affect the local excitation energies. The off-diagonal parameter $\delta = -14.7$ meV gives the trigonal splitting $\delta_{\rm tri} = 3|\delta| \approx 44$ meV. Figure S4(b) sketches the splitting of the t_{2g} manifold for the two signs of δ together with the t_{2g}^5 filling. In the absence of SOC, compression ($\delta < 0$) puts the a_{1g} singlet below the e_g^π doublet, so the t_{2g} hole occupies the e_g^π doublet. This doublet has $L_z = \pm 1$ for the component L_z of $L_{\rm eff}$ along [111]. An elongation ($\delta > 0$) reverses the order and would place the hole in the a_{1g} ($L_z = 0$) orbital.

Figure S5 summarizes the interplay of SOC and the trigonal field. In the cubic limit $\delta = 0$, the six spin-orbital eigenstates form a $J_{\rm eff} = 1/2$ ground doublet and a $J_{\rm eff} = 3/2$ quartet separated by $3\lambda/2$. In the phase convention used here, these ideal states are

$$\begin{aligned}
\left|\tfrac{1}{2}, \tfrac{1}{2}\right\rangle &= \tfrac{1}{\sqrt{3}} \left(-|d_{xy}\uparrow\rangle - i|d_{xz}\downarrow\rangle - |d_{yz}\downarrow\rangle\right), \\
\left|\tfrac{1}{2}, -\tfrac{1}{2}\right\rangle &= \tfrac{1}{\sqrt{3}} \left(\,|d_{xy}\downarrow\rangle + i|d_{xz}\uparrow\rangle - |d_{yz}\uparrow\rangle\right), \\
\left|\tfrac{3}{2}, \tfrac{3}{2}\right\rangle &= -\tfrac{1}{\sqrt{2}} \left(i|d_{xz}\uparrow\rangle + |d_{yz}\uparrow\rangle\right), \\
\left|\tfrac{3}{2}, \tfrac{1}{2}\right\rangle &= \tfrac{1}{\sqrt{6}} \left(2|d_{xy}\uparrow\rangle - i|d_{xz}\downarrow\rangle - |d_{yz}\downarrow\rangle\right), \\
\left|\tfrac{3}{2}, -\tfrac{1}{2}\right\rangle &= \tfrac{1}{\sqrt{6}} \left(2|d_{xy}\downarrow\rangle - i|d_{xz}\uparrow\rangle + |d_{yz}\uparrow\rangle\right), \\
\left|\tfrac{3}{2}, -\tfrac{3}{2}\right\rangle &= \tfrac{1}{\sqrt{2}} \left(-i|d_{xz}\downarrow\rangle + |d_{yz}\downarrow\rangle\right).
\end{aligned} \tag{S2}$$

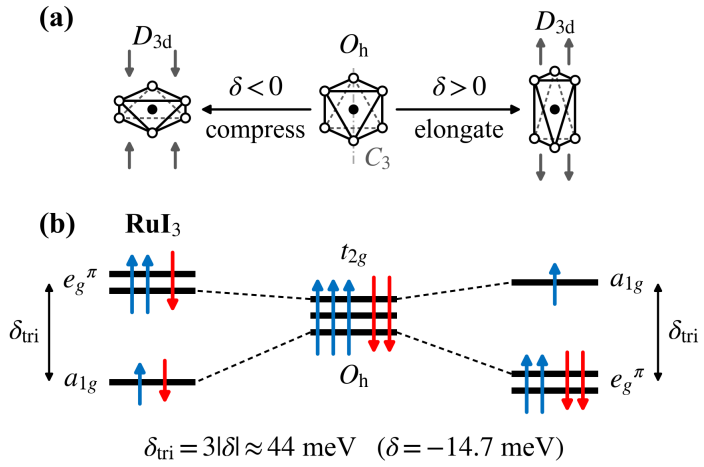

Figure S4. Trigonal crystal field of the RuI_6 octahedron. (a) Compression ($\delta < 0$, left) and elongation ($\delta > 0$, right) along the C_3 axis, which lower the symmetry of the octahedron from O_h (center) to D_{3d}. The filled circle is Ru and the open circles are I. (b) The resulting t_{2g} levels [Eq. (2) of the main text] split by $\delta_{tri} = 3|\delta|$. Arrows show the t_{2g}^5 filling, and the empty slot is the hole.

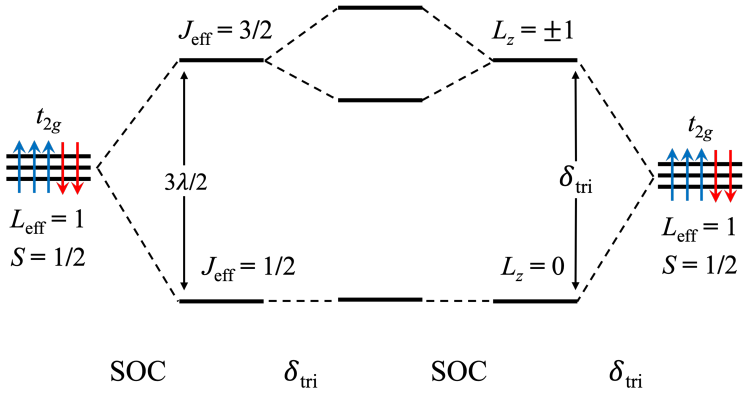

Figure S5. Spin-orbital levels of the low-spin t_{2g}^5 ($S = 1/2$, $L_{eff} = 1$) Ru^{3+} ion, with SOC and the trigonal field δ_{tri} applied in either order. Left: SOC splits the manifold into the $J_{eff} = 1/2$ doublet and the $J_{eff} = 3/2$ quartet separated by $3\lambda/2$, and δ_{tri} splits the quartet. Right: δ_{tri} splits the t_{2g} levels into $L_z = 0$ and $L_z = \pm 1$, and SOC mixes them.

The exact diagonalization (ED) ground state projects onto the ideal $J_{eff} = 1/2$ doublet with a weight of ≈ 0.99, and the small deviation from unity is due to the weak $J_{eff} = 1/2$–$J_{eff} = 3/2$ mixing induced by the finite trigonal distortion ($\delta = -14.7$ meV).

V. Hopping channels

The four symmetry-inequivalent 1NN t_{2g}–t_{2g} hopping channels t_1–t_4 are visualized through the overlapping Wannier functions in Fig. S6, and their Slater–Koster forms and *ab initio* values are given in Fig. S7. The 1NN, second-nearest-neighbor (2NN) and third-nearest-neighbor (3NN) bonds are at the Ru–Ru distances $d = 4.046$, 7.008 and 8.092 Å, and the values of their hopping channels are given with Eqs. (4) and (5) of the main text. Together with the on-site trigonal parameter δ and the interaction parameters U, J_H and λ, they are the complete input of Eq. (3) of the main text.

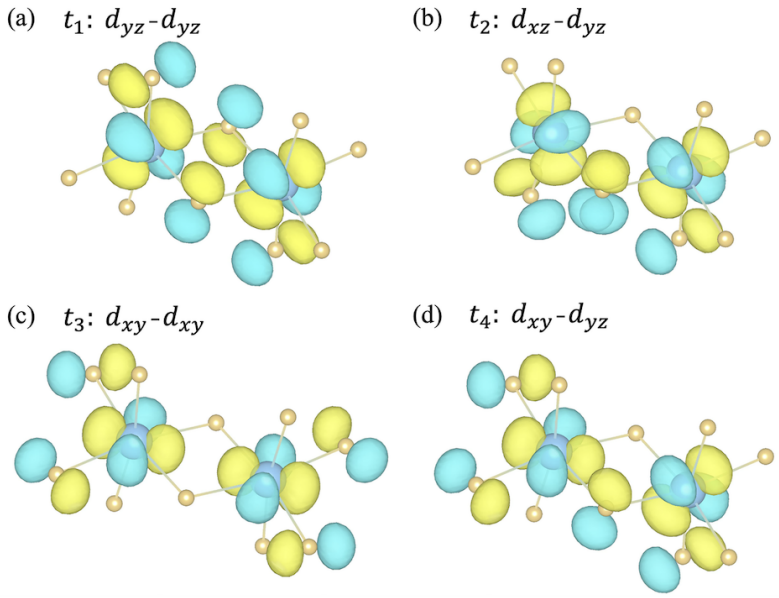

Figure S6. The four 1NN t_{2g}–t_{2g} hopping channels of RuI_3 shown by the overlapping Wannier functions: (a) t_1, d_{yz}–d_{yz}; (b) t_2, d_{xz}–d_{yz} via the bridging I 5p orbital; (c) t_3, d_{xy}–d_{xy}; (d) t_4, d_{xy}–d_{yz}.

In the basis (d_{xz}, d_{yz}, d_{xy}) the Z-bond matrix of the 1NN, 2NN and 3NN bonds is $T_Z = [[t_1,\ t_2 + a_1,\ t_4 + a_2],\ [t_2 - a_1,\ t_1,\ t_4 - a_2],\ [t_4 - a_2,\ t_4 + a_2,\ t_3]]$, whose symmetric part is the four-parameter form of Eq. (4) of the main text. The 1NN and 3NN bonds have an inversion center at their midpoint, which makes their matrices symmetric ($a_1 = a_2 = 0$). They also have a twofold axis along the bond, which exchanges d_{xz} and d_{yz} and gives the symmetric part its four-parameter form. The 2NN bond has no inversion center but has a twofold axis perpendicular to it, along the 1NN Z bond of the site between the two 2NN sites. This axis exchanges d_{xz} and d_{yz} and keeps the symmetric part in the same form. The antisymmetric part with a_1 and a_2 remains and generates the 2NN Dzyaloshinskii–Moriya (DM) vector. The values of Eq. (5) of the main text are those of the bond between A-sublattice sites whose bond vector points along $[\bar{1}\bar{1}2]$, the in-plane projection of the cubic $+z$ axis. The reversed bond carries the transpose. The B-sublattice bonds are related to the A bonds by the inversion at the 1NN bond center and carry the same matrix for the bond vector along $[11\bar{2}]$. The same rules fix the DM vector of Eq. (6) of the main text. For the Z-type bond so directed, the six-site value is $\mathbf{D} = (0.59, 0.59, 1.04)$ meV in the cubic axes, with $D^x = D^y$ as the twofold axis requires. This vector has components of 1.28 meV along c and 0.37 meV along the bond. The X- and Y-type bonds carry the cyclic permutations (1.04, 0.59, 0.59) and (0.59, 1.04, 0.59) meV, and the reversed bond carries $-\mathbf{D}$. Each of the 1NN, 2NN and 3NN bonds is assigned to its Kitaev axis by the orbital that carries t_3. On the Z bonds, the diagonal entry that differs from the other two lies on d_{xy}. The X and Y bonds of the three neighbor distances follow by cyclic permutation of the orbitals, which we verified against the Wannier output to 1×10^{-4} meV.

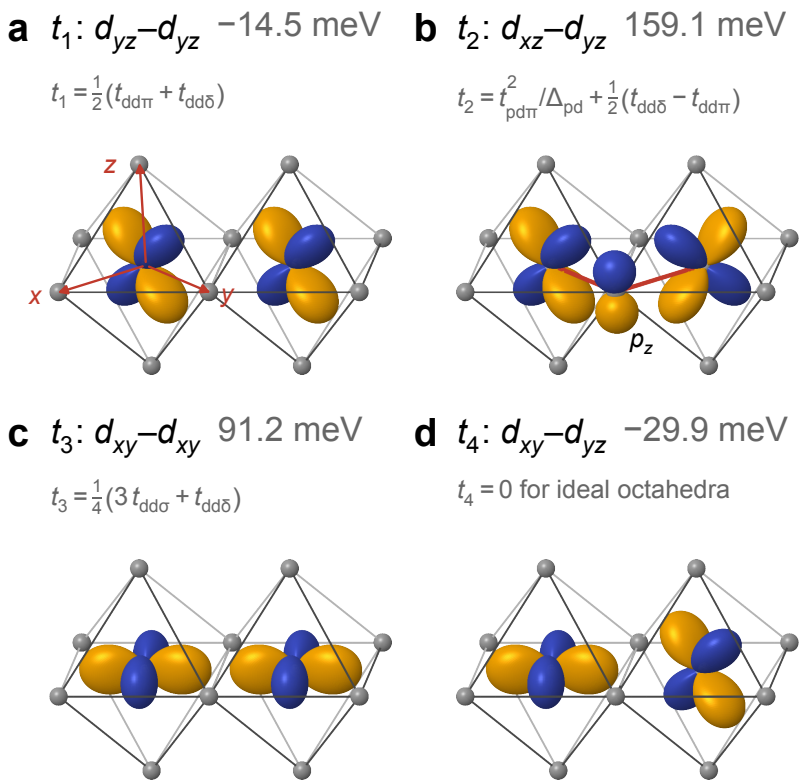

Figure S7. The four 1NN t_{2g}–t_{2g} hopping channels t_1–t_4 of the Z bond with their *ab initio* values and Slater–Koster forms.

VI. Two-site ED and the pseudospin projection

We diagonalize Eq. (3) of the main text in the full $\binom{12}{2} = 66$-dimensional two-hole Fock space. The spectrum contains three characteristic energy scales [Fig. S8(a)]. The lowest four states span 7.34 meV, and the gap above this manifold is 201.15 meV. States dominated by double occupancy appear near 1.3 eV. The gap-to-width ratio of 27 supports a low-energy pseudospin projection.

Resolved by local-doublet content, the lowest four states have an average weight of 97.6% on product states of the local ground doublets, with individual values from 96.8% to 98.2%. The remaining weight lies on doubly occupied states (2.0%) and on excited local doublets (0.5%).

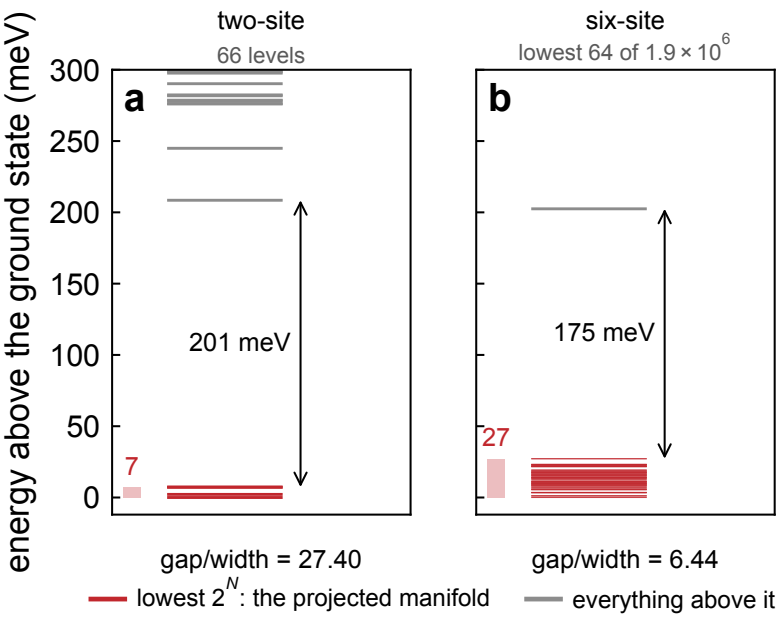

Figure S8. Energy levels of (a) all 66 eigenstates of the two-site cluster and (b) the six-site bridge cluster. Red: the lowest 2^N states, which the pseudospin model represents; gray: the states above them. The bar at the left gives the width of the red manifold and the arrow the gap to the next state. In (b) the red levels are those of the projected pseudospin Hamiltonian and the gap is the ED value.

VII. Finite clusters and the extraction of the exchange couplings

Figure S9 shows the finite clusters used in this work. The three electronic clusters in panels (a)–(c) share one procedure. Each Ru site carries the single-ion Hamiltonian of Sec. IV, including the on-site interaction. Each bond is coupled by its Wannier hopping matrix (Sec. V). We diagonalize the resulting Hamiltonian at one hole per Ru. Its lowest 2^N eigenstates are projected onto the product states of the ideal cubic $J_{\rm eff} = 1/2$ doublets of Eq. (S2) and symmetrically orthonormalized. The bilinear part of the resulting pseudospin Hamiltonian is then extracted bond by bond in the form of Eq. (6) of the main text. The two-site cluster (a) contains only the exchange paths that connect the two sites directly (Sec. VI). The bridge (b) and hexagon (c) clusters [4] add the paths through intermediate Ru sites and give the six-site couplings of Table 1 of the main text. The 1NN tensor is read from the central bond of the bridge, and the 2NN and 3NN tensors are read from the hexagon. The sites are numbered as in the cluster expansions below, so that the subclusters $\{1, 2, 3\}$, ... listed there can be read off directly. The 24-site cluster (d) is the lattice on which the pseudospin model assembled from these couplings is solved (Sec. IX).

The six-hole Hamiltonian has the dimension $\binom{36}{6} = 1\,947\,792$ and 1.9×10^8 nonzero elements. Its lowest 65 states are obtained by Chebyshev-filtered subspace iteration until the residual of every state is below 10^{-6}. The 64 states of the pseudospin manifold are separated from the 65th by 175 meV (bridge) and 170 meV (hexagon). The part of the projected Hamiltonian that no bilinear term can represent has a root-mean-square size of 0.05 meV (bridge) and 0.09 meV (hexagon). On the bridge the 64 states span 27.2 meV, and the projected pseudospin Hamiltonian reproduces this width to 0.01 meV (Fig. S8b). The central bond of the bridge is the only bond of either cluster with its full set of 1NN paths and an inversion center inside the cluster. On this bond the fitted $\mathbf{D}$ vanishes to 10^{-5} meV, as inversion requires. The four outer bridge bonds and the six 1NN bonds of the hexagon acquire an artificial $\mathbf{D}$ of 0.3 to 0.4 meV and a Kitaev coupling larger in magnitude by about 1.0 meV, and they are not used. The hopping-channel decomposition is given in Table S1 and drawn in Fig. S10. Table S2 applies the same procedure to α-$RuCl_3$ with the published inputs [4]. The 1NN and 3NN couplings reproduce Table IV of that work to 0.05 and 0.06 meV. On the 2NN bond, Γ agrees to 0.02 meV and $|\mathbf{D}|$ to 0.1 meV, whereas J, K and Γ' differ by 0.3 to 0.5 meV. The uncertainty of the published values from the choice of the projection basis is estimated at ± 1 meV [4]. For Na_2IrO_3 the same bridge and hexagon give $(J_1, K_1, \Gamma_1, \Gamma_1') = (1.60, -17.93, -0.06, -1.79)$ meV and $J_3 = 6.91$ meV against $(1.6, -17.9, -0.1, -1.8)$ and 6.8 meV in Table III of that work.

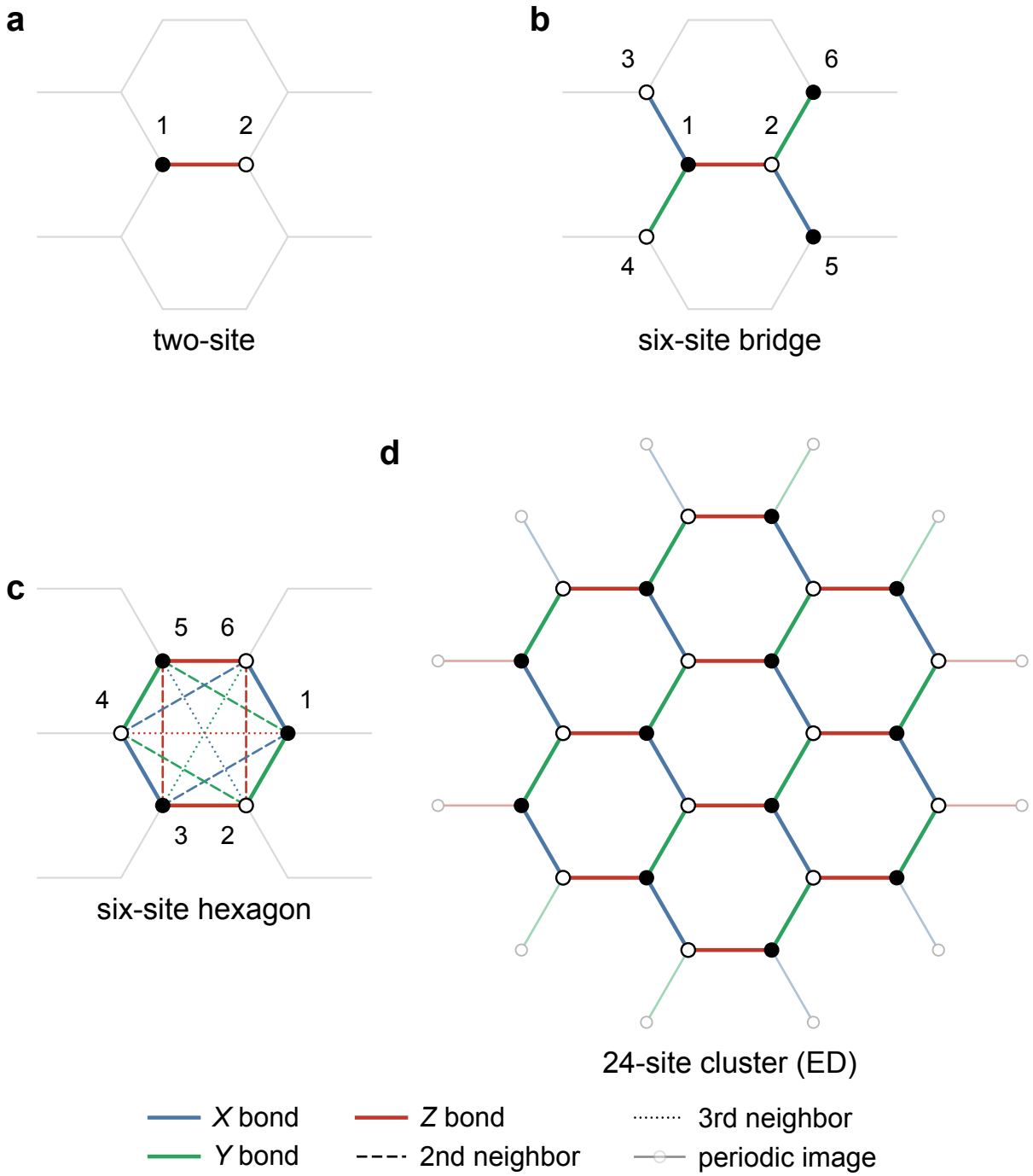

Figure S9. Clusters used for the exchange couplings and the pseudospin ED, drawn as in Fig. 1 of the main text. Filled and open disks mark the two sublattices, and light-gray lines show the surrounding honeycomb lattice. The site numbers of (a)–(c) are also used in the cluster expansions below. (a) The two-site cluster. (b) The six-site bridge and (c) the six-site hexagon cluster [4]. (d) The 24-site periodic cluster of the pseudospin ED. Faint bonds close the periodic boundary and end on open gray circles at the periodic images.

Table S1. Channel decomposition of the six-site couplings of monolayer RuI_3 (meV). The cluster is diagonalized with only the listed hopping matrices, where $T^{(1)}$, $T^{(2)}$ and $T^{(3)}$ are the complete 1NN, 2NN and 3NN hopping matrices (Sec. V). The 1NN couplings are for the central bond of the bridge cluster and the 2NN and 3NN couplings for the Z bonds of the hexagon. The two-site values of Table 1 of the main text are listed for comparison.

	hoppings on	J	K	Γ	Γ'	$\lvert\mathbf{D}\rvert$
1NN	two-site	−1.62	−7.11	−3.98	−3.47	0
	$T^{(1)},T^{(2)},T^{(3)}$ (all)	−1.43	−4.84	−3.95	−3.33	0
	$T^{(2)},T^{(3)}$ (no $T^{(1)}$)	0.00	0.00	0.00	0.00	0
	$T^{(1)},T^{(3)}$ (no $T^{(2)}$)	−2.06	−5.89	−4.21	−3.71	0
	$T^{(1)},T^{(2)}$ (no $T^{(3)}$)	−1.41	−4.85	−3.93	−3.30	0
	$T^{(1)}$ only	−2.04	−5.89	−4.17	−3.65	0
	$T^{(2)}$ only	0.00	0.00	0.00	0.00	0
	$T^{(3)}$ only	0.00	0.00	0.00	0.00	0
2NN	two-site	−1.58	1.82	1.17	1.81	1.42
	$T^{(1)},T^{(2)},T^{(3)}$ (all)	−0.62	0.86	0.51	0.80	1.34
	$T^{(2)},T^{(3)}$ (no $T^{(1)}$)	−1.36	1.48	1.17	1.73	1.50
	$T^{(1)},T^{(3)}$ (no $T^{(2)}$)	−0.19	0.27	0.09	0.16	0.18
	$T^{(1)},T^{(2)}$ (no $T^{(3)}$)	−0.04	0.68	0.19	0.28	1.57
	$T^{(1)}$ only	−0.19	0.32	0.40	0.51	0.77
	$T^{(2)}$ only	−1.35	1.48	1.16	1.72	1.52
	$T^{(3)}$ only	0.00	0.00	0.00	0.00	0
3NN	two-site	0.95	0.00	0.01	−0.18	0
	$T^{(1)},T^{(2)},T^{(3)}$ (all)	4.53	0.09	−0.06	−0.29	0
	$T^{(2)},T^{(3)}$ (no $T^{(1)}$)	0.97	0.01	0.01	−0.18	0
	$T^{(1)},T^{(3)}$ (no $T^{(2)}$)	0.93	0.02	−0.03	−0.23	0
	$T^{(1)},T^{(2)}$ (no $T^{(3)}$)	0.94	−0.01	0.01	−0.03	0
	$T^{(1)}$ only	0.01	0.00	0.01	0.00	0
	$T^{(2)}$ only	0.00	0.00	0.00	0.00	0
	$T^{(3)}$ only	0.95	0.00	0.01	−0.18	0

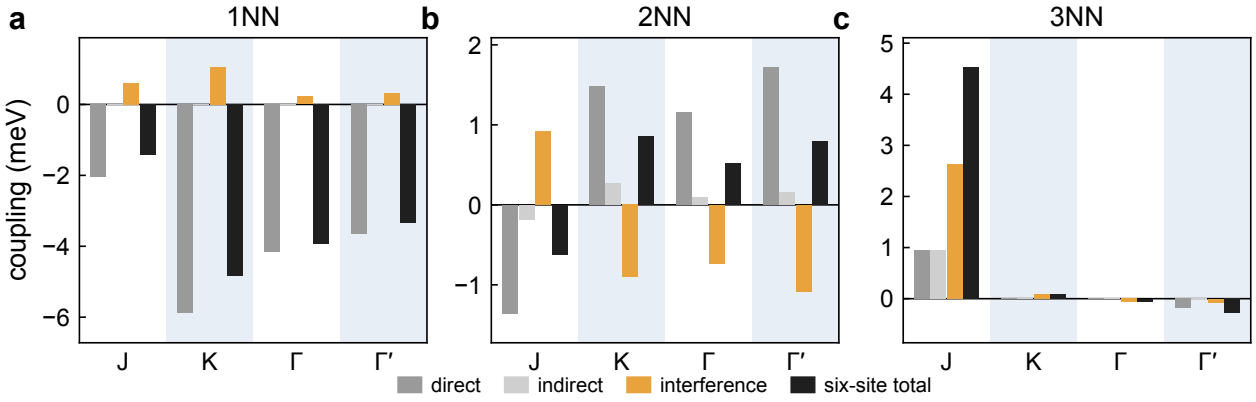

Figure S10. Channel decomposition of Table S1 drawn as bars. For (a) 1NN, (b) 2NN and (c) 3NN, each of J, K, Γ and Γ' is split into the direct part (only the hopping matrix of the bond itself), the indirect part (that matrix removed) and the interference part (the remainder). The six-site total is shown alongside.

Table S2. Six-site couplings of α-$RuCl_3$ (meV) on the 1NN, 2NN and 3NN Z bonds, compared with the published values rounded to 0.1 meV [4]. Our calculation uses the hopping, crystal-field and interaction parameters of that work ($U = 3.0$ eV, $J_H = 0.6$ eV, $\lambda = 0.15$ eV).

		J	K	Γ	Γ'	$\lvert\mathbf{D}\rvert$
1NN Z	this work	−2.20	−5.02	8.03	−0.95	0
	published [4]	−2.2	−5.0	8.0	−1.0	0
2NN Z	this work	−0.22	−0.41	0.58	0.68	0.66
	published [4]	0.1	−0.9	0.6	0.3	0.57
3NN Z	this work	2.46	0.31	−0.14	−0.08	0
	published [4]	2.4	0.3	−0.1	−0.1	0

The decomposition in Table S1 identifies which hopping matrices are required for each contribution. The large enhancement of J_3 disappears when any one of the three matrices is removed. This dependence is consistent with virtual paths around the 1–3–4 triangle, which contains a 1NN, a 2NN and a 3NN bond.

The 1NN and 2NN interference parts survive without $T^{(3)}$ and mainly involve the triangles with two 1NN bonds and one 2NN bond, such as 6–1–2. The signs of the interference parts differ between the 1NN, 2NN and 3NN bonds: interference reduces the magnitude of K_1 by 1.05 meV, reduces the 2NN symmetric couplings, and enhances J_3. With only $T^{(1)}$, the 3NN Heisenberg coupling is 0.007 meV. Including both $T^{(1)}$ and $T^{(2)}$ raises it to 0.94 meV. Removing $T^{(3)}$ also changes J_2 from −0.62 to −0.04 meV. For α-$RuCl_3$, this removal reduces J_3 from 2.46 to 0.46 meV.

The cluster expansion of Figs. S11–S13 resolves the multisite renormalization of the 1NN, 2NN and 3NN couplings by cluster size. Every subcluster S of the six-site cluster that contains the target bond is diagonalized with all hopping matrices inside S, and the exchange tensor $J(S)$ is extracted as for the six-site cluster. The part of the coupling that first appears on S is the cumulant $W(S) = \sum_{S' \subseteq S} (-1)^{|S|-|S'|} J(S')$, where the sum runs over the subclusters S' that contain this bond. The cumulants of all 16 subclusters add up to the six-site value. The percentages quoted here and in the figures are shares of the total cumulant weight $\sum_S |W(S)|$, counted positive when the cumulant has the sign of the six-site value and negative when it works against it. They stay within ±100% also when the series alternates. The expansion is done component by component of (J, K, Γ, Γ') and also of the DM vector $\mathbf{D}$ on the 2NN bond. For the 1NN Z bond $(1, 2)$ of the bridge cluster (Fig. S11) the two-site cluster gives $K = -7.11$ meV. Each of the four three-site clusters $\{1, 2, k\}$ contains the Z bond, one further 1NN bond and the 2NN bond that closes the triangle. They give +0.64 meV each and +2.57 meV in total. The six four-site clusters give −0.30 meV, the five-site clusters −0.01 meV and the six-site bridge −0.001 meV, so $K_1 = -4.84$ meV. The corrections to J, Γ and Γ' beyond the two-site cluster are +0.19, +0.04 and +0.13 meV. The reduction of the magnitude of K_1 from its two-site value therefore comes mainly from the three-site clusters. Part of this reduction is present with the 1NN hopping alone, where the six-site value is −5.89 meV (Table S1). The 2NN hopping on the triangle reduces the magnitude of K_1 further. The 2NN Z bond $(6, 2)$ of the hexagon (Fig. S12) is the bond of Table S1. For this bond, the two-site cluster gives $(J, K, \Gamma, \Gamma') = (-1.58, 1.82, 1.17, 1.81)$ meV and $|\mathbf{D}| = 1.42$ meV. Among the three-site clusters, the triangle $\{1, 2, 6\}$ dominates with $(+1.73, -1.38, -1.02, -1.66)$ meV. It joins sites 6 and 2 by two 1NN bonds through their common neighbor 1. The other three triangles lie between −0.37 and +0.47 meV. The four-site clusters partly restore the two-site values with $(-0.36, +0.57, -0.25, -0.13)$ meV. The five-site clusters contribute at most 0.17 meV and the six-site hexagon at most 0.01 meV, which gives the six-site values $(-0.62, 0.86, 0.51, 0.80)$ meV. The DM vector behaves differently. Projected on the direction of the six-site $\mathbf{D}$, the two-site cluster gives 1.42 meV, the three-site clusters −0.52 meV and the four-site clusters +0.41 meV. Hence $|\mathbf{D}| = 1.34$ meV is set by the direct 2NN hopping. The symmetric part of the 2NN tensor is thus reduced by about a factor of two by the 1NN–1NN path through the common neighbor, while $\mathbf{D}$ is a two-site property.

For the 3NN bond $(1, 4)$ of the hexagon (Fig. S13) the two-site cluster gives 0.95 meV, 20% of $\sum_S |W(S)| = 4.79$ meV. Each of the four triangles contains a 1NN, a 2NN and a 3NN bond and gives 0.70 meV. Together they give 2.81 meV (59%). The six four-site clusters give 0.87 meV (18%), most of it from the two clusters that contain a second 3NN bond (0.35 meV each). The two four-site chains around half of the hexagon give only −0.01 meV each, so paths of 1NN hops alone do not contribute. The five-site clusters and the six-site hexagon give −0.12 and +0.02 meV. The expansion therefore converges within the hexagon. The three-site interference of $T^{(1)}$, $T^{(2)}$ and $T^{(3)}$ on the triangle dominates J_3, followed by the connected four-site processes in the clusters that contain a second 3NN bond. Switching the hopping matrices $T^{(1)}$, $T^{(2)}$ and $T^{(3)}$ on and off inside every subcluster and inverting over both sites and matrices resolves the direct, indirect and interference parts of Table S1 by sites. The 112 combinations add up to the six-site value. Of the interference part, 2.45 of 2.63 meV lies on the four triangles as the channel that needs all three matrices. Of the indirect part, 0.82 of 0.94 meV lies on the six four-site clusters and comes from connected

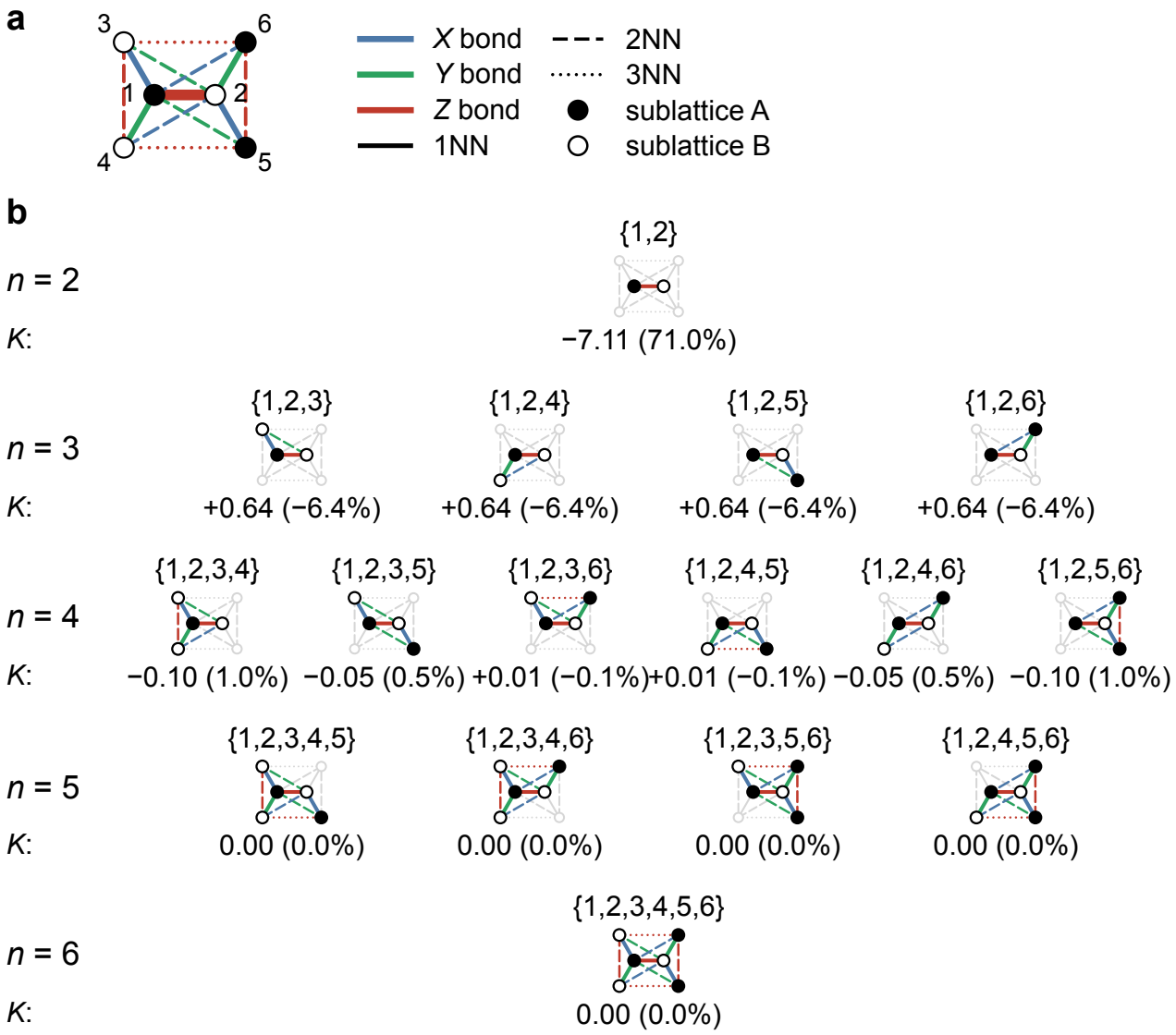

c

	$n = 2$	$n = 3$	$n = 4$	$n = 5$	$n = 6$	six-site
J	−1.62 (84.1%)	+0.05 (−2.8%)	+0.10 (−4.9%)	+0.04 (−1.9%)	0	−1.43
K	−7.11 (71.0%)	+2.57 (−25.7%)	−0.30 (3.0%)	−0.01 (0.1%)	0	−4.84
Γ	−3.98 (97.9%)	+0.04 (−0.9%)	+0.01 (−0.3%)	−0.01 (0.3%)	0	−3.95
Γ'	−3.47 (91.9%)	+0.18 (−4.9%)	−0.03 (0.7%)	−0.02 (0.6%)	0	−3.33

Figure S11. Cluster expansion of the 1NN exchange tensor of monolayer RuI_3 on the bridge cluster. (a) The bridge drawn as in Fig. S9, with the tensor read on the central Z bond $(1, 2)$ (thick line). (b) The 16 subclusters that contain sites 1 and 2, arranged in one row per cluster size n. The bonds inside each subcluster are in color and the rest in gray. The number under each subcluster is its cumulant of K in meV, and the number in parentheses is its share of the total cumulant weight $\sum_S |W(S)|$. The share is positive when the cumulant has the sign of the six-site value. (c) The cumulants of J, K, Γ and Γ' summed over the subclusters of each size, in meV with their shares. The last column is the six-site value.

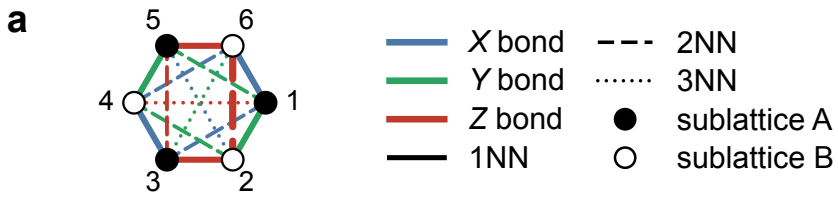

b

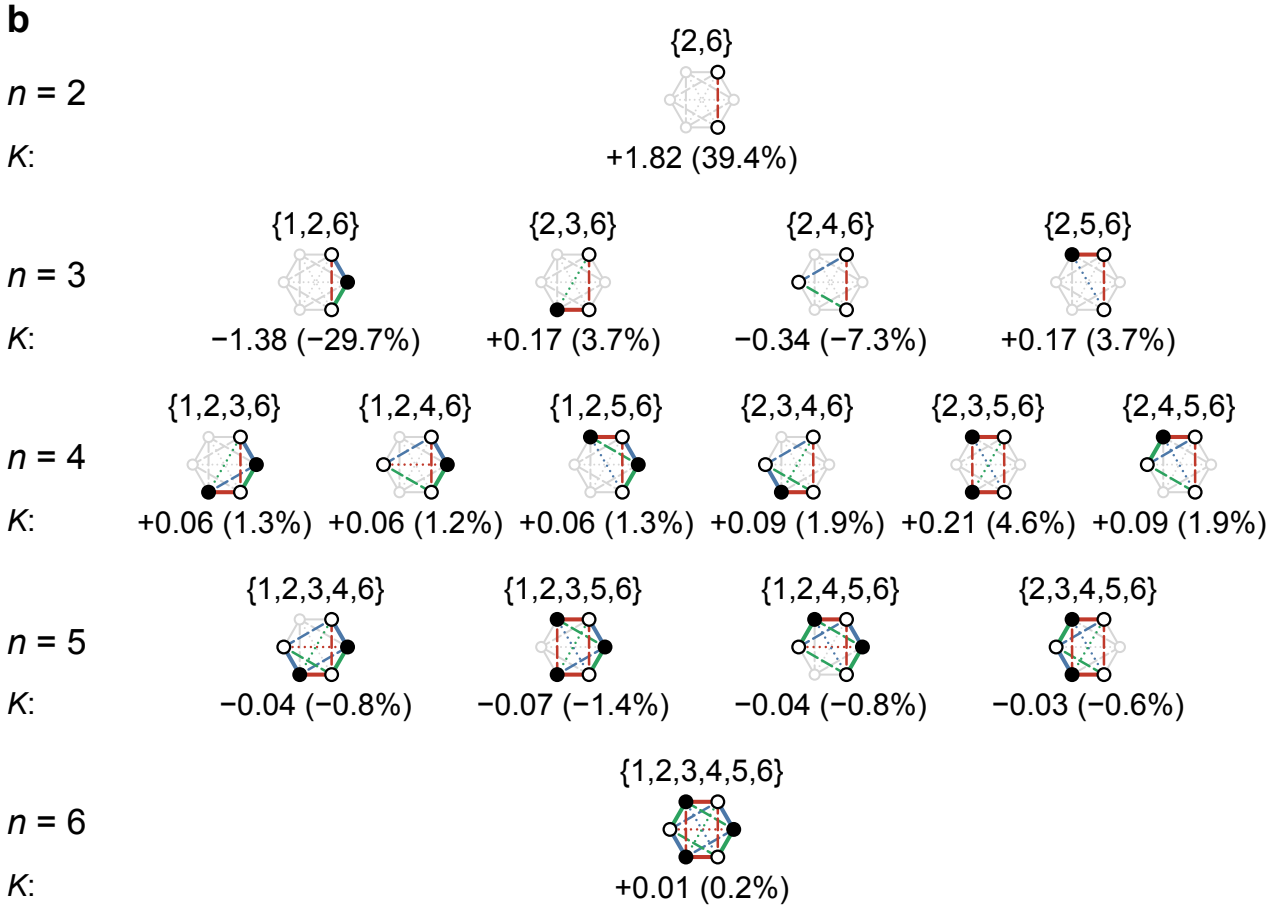

c

	$n = 2$	$n = 3$	$n = 4$	$n = 5$	$n = 6$	six-site
J	−1.58 (33.3%)	+1.22 (−25.8%)	−0.36 (7.7%)	+0.10 (−2.2%)	−0.01 (0.2%)	−0.62
K	+1.82 (39.4%)	−1.37 (−29.6%)	+0.57 (12.2%)	−0.17 (−3.7%)	+0.01 (0.2%)	+0.86
Γ	+1.17 (33.8%)	−0.36 (−10.6%)	−0.25 (−7.2%)	−0.04 (−1.1%)	0	+0.51
Γ'	+1.81 (34.6%)	−0.80 (−15.3%)	−0.13 (−2.5%)	−0.08 (−1.6%)	0	+0.80
$D \cdot \hat{D}$	+1.42 (43.4%)	−0.52 (−15.9%)	+0.41 (12.4%)	+0.02 (0.7%)	+0.01 (0.4%)	1.34

Figure S12. Cluster expansion of the 2NN exchange tensor of monolayer RuI_3 on the hexagon cluster, drawn as Fig. S11. (a) The tensor is read on the 2NN Z bond $(6, 2)$ (thick dashed line). (b) The 16 subclusters that contain sites 2 and 6, with the cumulant of K under each. (c) The cumulants of J, K, Γ, Γ' and $\mathbf{D} \cdot \hat{\mathbf{D}}$ summed over the subclusters of each size, where $\hat{\mathbf{D}}$ is the direction of the six-site DM vector. The last column is the six-site value.

four-site processes with 1NN and 2NN hops. These contributions are 0.18 meV each on $\{1,2,4,5\}$ and $\{1,3,4,6\}$, 0.14 meV each on $\{1,2,4,6\}$ and $\{1,3,4,5\}$, and 0.09 meV each on the two chains $\{1,2,3,4\}$ and $\{1,4,5,6\}$. The three consecutive 1NN hops of the two chains are compensated in the full expansion by an interference part of -0.10 meV. For all three couplings the cumulants of the five-site clusters and of the six-site cluster stay below 0.2 meV, so the expansion converges within the six-site clusters.

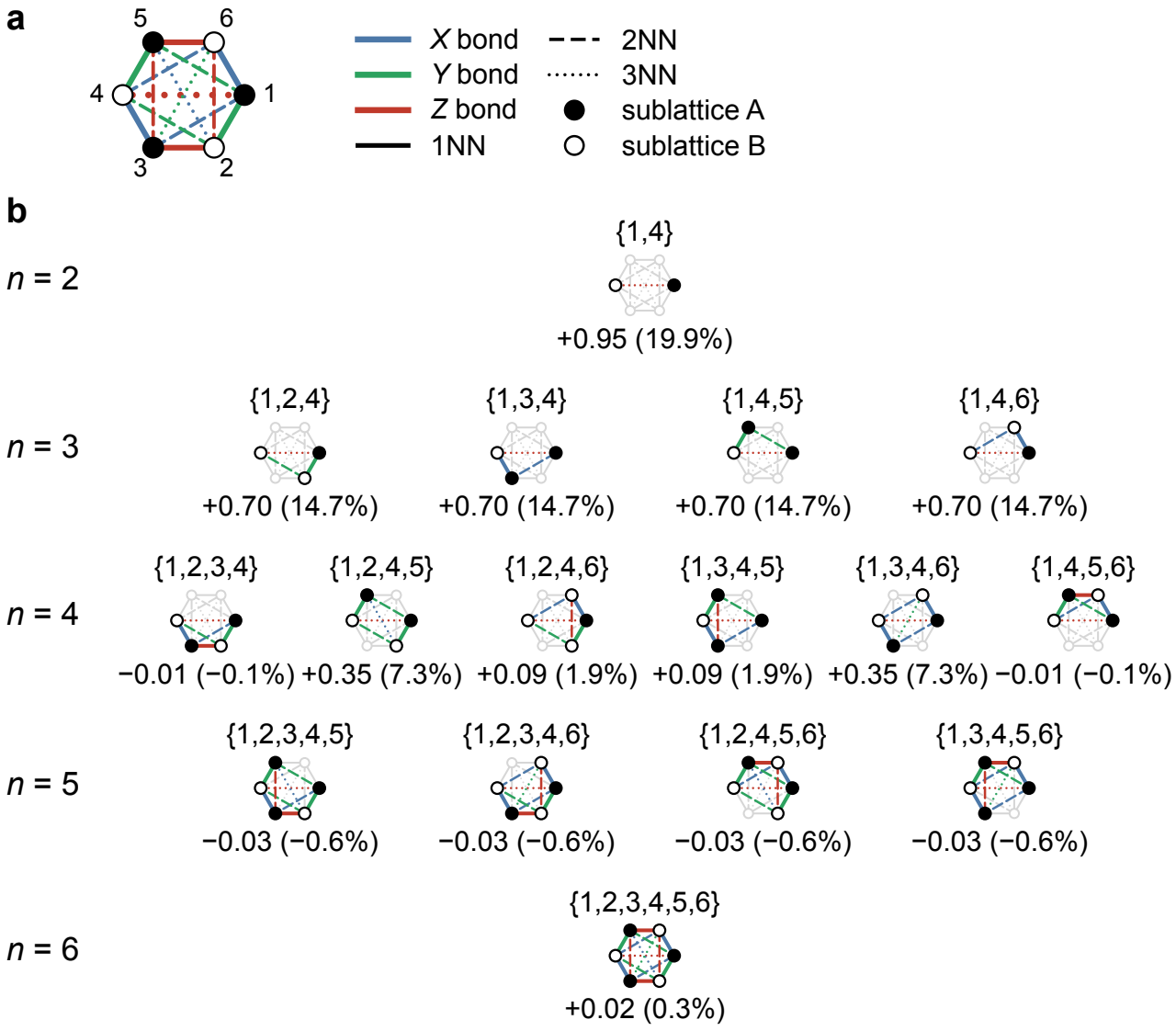

c

	$n=2$	$n=3$	$n=4$	$n=5$	$n=6$	six-site
J	+0.95 (19.9%)	+2.81 (58.7%)	+0.87 (18.1%)	−0.12 (−2.4%)	+0.02 (0.3%)	+4.53

Figure S13. Cluster expansion of the 3NN Heisenberg coupling J_3 of monolayer RuI_3 on the hexagon cluster, drawn as Fig. S11. (a) The coupling is read on the 3NN bond $(1,4)$ (thick dotted line). (b) The 16 subclusters that contain sites 1 and 4, with the cumulant $W(S)$ of J_3 under each. (c) The cumulants summed over the subclusters of each size. The last column is the six-site value.

VIII. Dependence of the six-site couplings on U, J_H and λ

Table S3 repeats the bridge and hexagon calculations with U between 1.5 and 2.5 eV, J_H between 0.20 and 0.40 eV and λ between 0.15 and 0.21 eV. One parameter is varied at a time around the set of Table 1 of the main text. The magnitudes of the leading 1NN couplings and J_3 increase as U decreases or J_H increases. The 2NN couplings do not follow a common monotonic trend. Across the tested SOC range, J_1 and the 1NN off-diagonal terms change more strongly than K_1. The ratio $J_3/|K_1|$ stays between 0.79 and 1.33. At every point, zigzag is the lowest of the four collinear states (ferromagnetic, Néel, zigzag and stripe, each at its optimal moment direction). The energy difference $E_{\rm zz} - E_{\rm N}$ ranges from -0.06 meV per site at $J_H = 0.20$ eV to -1.31 meV per site at $J_H = 0.40$ eV. The projection is controlled in the same way as for the parameters of Table 1 of the main text. The gap between the 64-state manifold and the 65th state is 95–219 meV against a manifold width of 15–66 meV, and the smallest overlap eigenvalue of the Löwdin projection is 0.58–0.87. The root-mean-square size of the part of the projected Hamiltonian that is not representable by bilinear terms is 0.02–0.5 meV, with the largest values at $U = 1.5$ eV.

Table S3. Six-site couplings (meV) for different interaction parameters. Each column uses the stated U, J_H and λ (eV) with the hopping and crystal field of RuI_3. The bold column is the set of Table 1 of the main text. $E_{\rm FM}$, $E_{\rm N}$ and $E_{\rm zz}$ are the classical energies per site ($|\mathbf{S}| = 1/2$) of the ferromagnetic, Néel and zigzag states of the pseudospin Hamiltonian with these 1NN, 2NN and 3NN couplings, each at its optimal moment direction.

Parameter set	1	**2**	3	4	5	6	7
U	1.50	**2.00**	2.50	2.00	2.00	2.00	2.00
J_H	0.30	**0.30**	0.30	0.20	0.40	0.30	0.30
λ	0.18	**0.18**	0.18	0.18	0.18	0.15	0.21
J_1	−2.82	**−1.43**	−0.76	−0.52	−2.85	−2.01	−1.01
K_1	−8.41	**−4.84**	−3.04	−2.62	−8.13	−4.97	−4.67
Γ_1	−7.79	**−3.95**	−2.32	−2.06	−6.94	−4.41	−3.58
Γ'_1	−6.74	**−3.33**	−1.92	−1.72	−5.95	−3.90	−2.90
J_2	−0.51	**−0.62**	−0.60	−0.66	−0.55	−0.61	−0.63
K_2	0.84	**0.86**	0.82	1.03	0.60	0.81	0.89
Γ_2	0.37	**0.51**	0.49	0.53	0.45	0.50	0.53
Γ'_2	0.59	**0.80**	0.78	0.89	0.61	0.76	0.83
$\lvert\mathbf{D}_2\rvert$	2.19	**1.34**	0.98	1.14	1.68	1.30	1.36
J_3	10.70	**4.53**	2.55	3.49	6.45	4.99	4.18
K_3	0.33	**0.09**	0.03	0.03	0.22	0.08	0.09
Γ_3	−0.26	**−0.06**	−0.02	−0.02	−0.16	−0.08	−0.04
Γ'_3	−0.78	**−0.29**	−0.14	−0.13	−0.59	−0.32	−0.26
$J_3/\lvert K_1\rvert$	1.27	**0.94**	0.84	1.33	0.79	1.00	0.90
$E_{\rm FM}$	−3.23	**−1.44**	−0.54	0.26	−4.11	−1.97	−1.03
$E_{\rm N}$	−5.39	**−2.75**	−1.86	−2.32	−3.56	−2.88	−2.66
$E_{\rm zz}$	−6.62	**−3.33**	−2.07	−2.39	−4.87	−3.67	−3.07

IX. Magnetic ground state and phase diagram

All pseudospin ED uses the 24-site periodic honeycomb cluster of Fig. S9(d), which closes on all three bond directions so that no Kitaev bond type is favored by the boundary. The ordered pattern in each window of the phase diagrams of the main text is identified from the static spin structure factor

$$S(\mathbf{q}) = \frac{1}{N} \sum_{i,j} \sum_{\alpha=x,y,z} \langle S_i^\alpha S_j^\alpha \rangle \, e^{i\mathbf{q}\cdot(\mathbf{r}_i - \mathbf{r}_j)}, \tag{S3}$$

evaluated in the ED ground state with all three spin components included. Figure S14 shows the real-space pattern and $S(\mathbf{q})$ at the center of each window of Figs. 4(a) and 4(b) of the main text. The ordered states are distinguished by the position of their Bragg peaks: ferromagnetic at the zone center, Néel at the corners of the second Brillouin

zone, 120° at the K points, and zigzag and stripe at the M points. On the C_3-symmetric cluster, the three domains of a zigzag or stripe state carry equal weight. Zigzag and stripe are therefore distinguished by their collinear order parameters $m_P^2 = N^{-2}\sum_{ij}\epsilon_i^P\epsilon_j^P\langle\mathbf{S}_i\cdot\mathbf{S}_j\rangle$, where $\epsilon_i^P = \pm 1$ are the signs of the pattern P on N sites. The helical windows have no Bragg peak at a high-symmetry point. Because their incommensurate pitch does not fit the cluster, their peak-to-average ratio $S_{\max}/\bar{S}$ is only 1.3–1.6, against 2.3–9.1 for the ordered phases. The Kitaev-region structure factors remain diffuse ($S_{\max}/\bar{S} = 1.2$–1.6). At the pure Kitaev points, correlations beyond nearest neighbors vanish, as required by the exact solution of the Kitaev model [5, 6]. Diffuse finite-cluster correlations alone do not establish a spin liquid away from those limits.

The phase boundaries in Figs. 4 and 5 of the main text are the peaks of $-d^2E_{\mathrm{GS}}/d\varphi^2$. The peaks in Fig. 5(a) are level crossings, whereas those in Figs. 5(b) and 5(c) are broad avoided crossings on the finite cluster. The weaker hump at $\varphi \approx 0.95\pi$ in Fig. 5(b) lies inside the zigzag window and marks no change of order. A dotted window edge in Fig. 4 of the main text marks a change of the dominant correlations without a peak of the curvature. Near the Néel–zigzag crossover the correlations on the neighbor shells that distinguish Néel from zigzag (1NN, 2NN, 4NN and 5NN) are fitted at every φ by a weight b of the correlations of the Néel windows ($\varphi = 0.55\pi$ and 1.65π) and $1-b$ of those of the zigzag window ($\varphi = 1.20\pi$). The weight b changes rapidly near the peaks. On the ED grid of Fig. 5(c), the fitted values at the two curvature peaks are 0.588 and 0.574 rather than exactly 1/2. The crossover regions hatched in Fig. 5 of the main text have the smaller of the weights b and $1-b$ between 0.1 and 0.5. At the RuI_3 point ($\varphi \approx 1.41\pi$), $b = 0.21$ in Fig. 5(c) and 0.05 in Fig. 5(b). These weights describe the correlations of the finite cluster, not phase fractions. At the RuI_3 point with the 1NN, 2NN and 3NN couplings, the 3NN and 6NN correlations are strongly antiferromagnetic (−0.359) and ferromagnetic (+0.239), whereas the magnitudes on the 1NN, 2NN, 4NN and 5NN shells are below 0.016. The RuI_3 point thus lies inside the finite-size smearing of the Néel–zigzag boundary at 1.48π.

Figures S15 and S16 show $S(\mathbf{q})$ at the center of every window of Figs. 4 and 5 of the main text. Each panel is titled with the window and the point. A window is labeled by the collinear pattern whose m_P^2 exceeds 0.10 and exceeds that of the runner-up by a factor of 1.5. Where no pattern meets this criterion, the window is labeled by the Bragg peak of $S(\mathbf{q})$, which is accepted only when it exceeds every other high-symmetry position by 35%. Where the correlations remain diffuse and connect continuously to the pure Kitaev limit, the window carries the Kitaev-region label. The crossover regions of Fig. 5 of the main text appear in Fig. S16 as panels with both the Néel and the zigzag peaks, and at the RuI_3 point (last panel) their peak intensities are comparable. This comparison differs from the weight b because the three zigzag domains contribute at different M points.

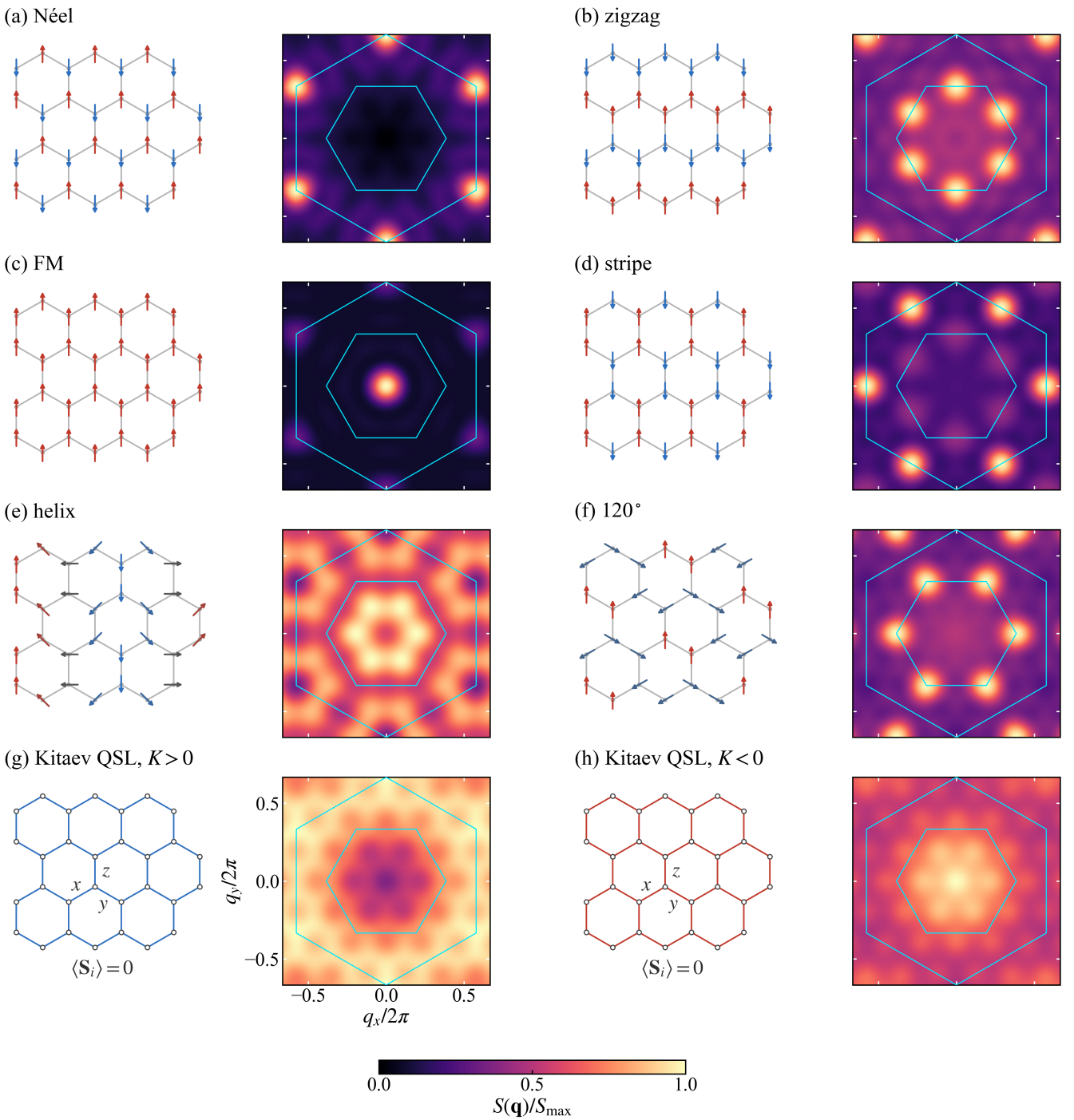

Figure S14. Correlation patterns of the phases in Fig. 4 of the main text: a schematic real-space pattern (left) and $S(\mathbf{q})/S_{\max}$ of the 24-site ED ground state (right) near the center of each window. (a) Néel (J-K, $\varphi = 0.25\pi$), (b) zigzag (J-K, 0.66π), (c) ferromagnetic (J-K, 1.13π), (d) stripe (J-K, 1.62π), (e) helix (J-K-Γ, 0.58π), (f) 120° (J-K-Γ, 1.66π), and the Kitaev windows of the J-K model at (g) $\varphi = \pi/2$ and (h) $\varphi = 3\pi/2$. In (g), $S(\mathbf{q})$ is averaged over the threefold degenerate ground state. The arrows are schematic reference spins colored by their vertical component. Panels (g) and (h) have no static moment, and their bonds are colored by the sign of the 1NN bond correlation and labeled by their Kitaev axis. Cyan lines mark the first and second Brillouin zones.

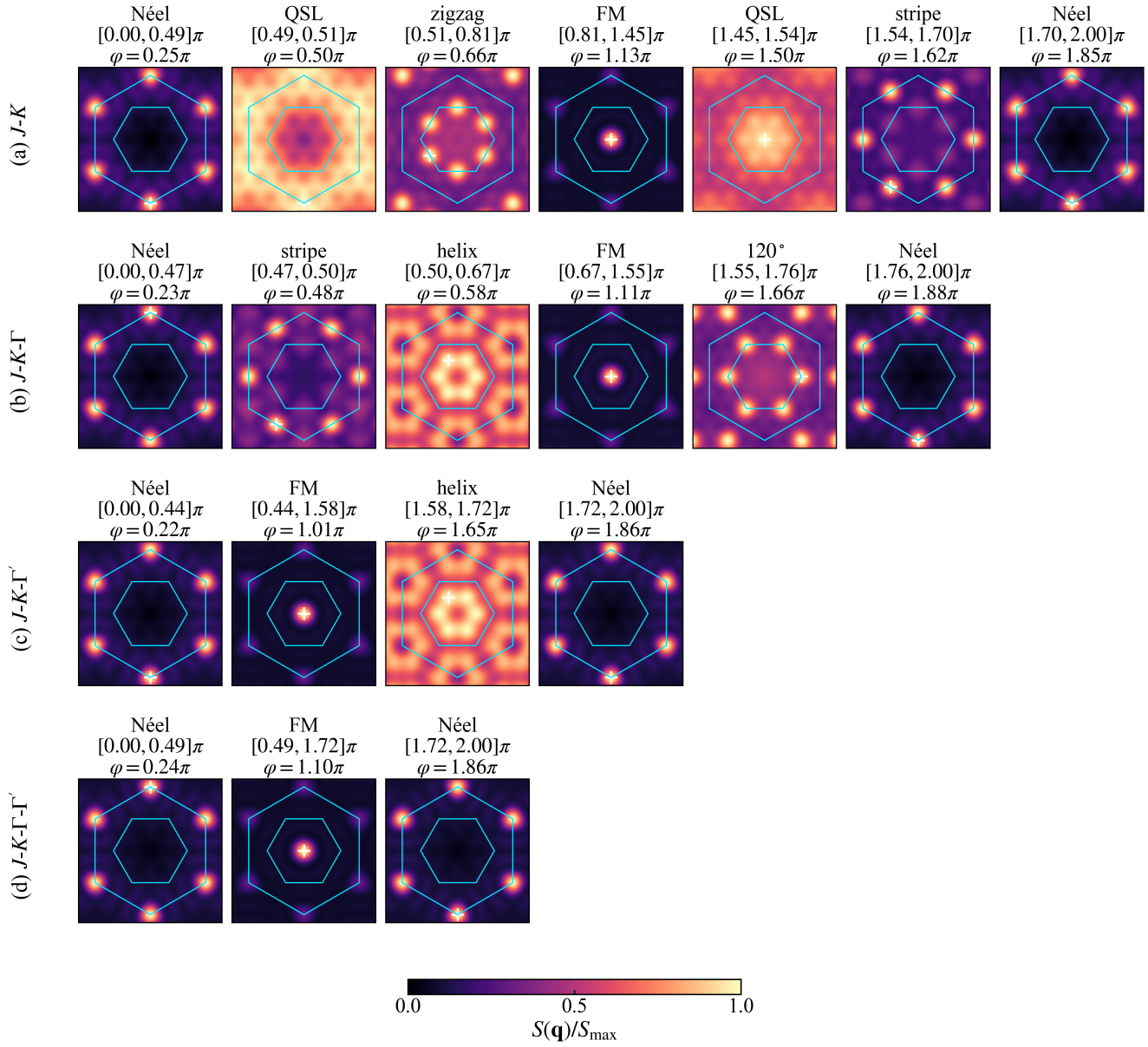

Figure S15. Static spin structure factor $S(\mathbf{q})/S_{\max}$ of the ED ground state at the center of every window of the 1NN phase diagrams of Fig. 4 of the main text, rows (a)–(d) as there. Each panel gives the window, its φ range and the point shown. The white cross marks the maximum, and cyan lines mark the first and second Brillouin zones.

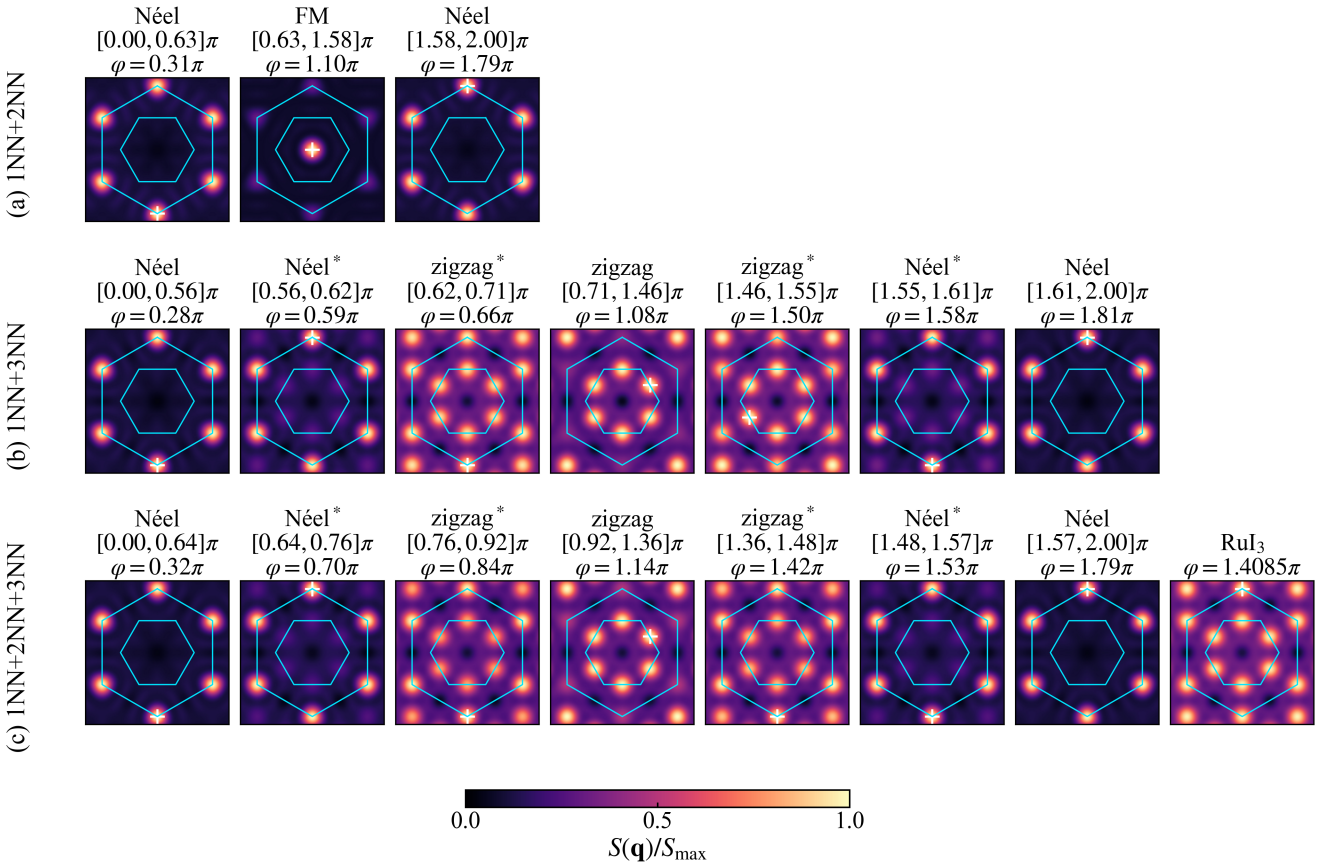

Figure S16. As Fig. S15, for the phase diagrams of Fig. 5 of the main text, rows (a)–(c) as there. Asterisks mark the Néel–zigzag crossover regions (Sec. IX), and the last panel of row (c) is RuI_3.

X. Density-matrix renormalization group

The density-matrix renormalization group (DMRG) calculations of the pseudospin Hamiltonian with the 1NN, 2NN and 3NN couplings use the periodic honeycomb clusters of Fig. S17, so that the size series starts from the ED cluster. A cluster with supercell vectors T_1 and T_2 admits a wave vector $\mathbf{q}$ only if $\mathbf{q} \cdot T_1$ and $\mathbf{q} \cdot T_2$ are multiples of 2π. The three M points are all present only when both supercell vectors have even coefficients, which restricts the admissible sizes to multiples of eight sites. Every cluster of Fig. S17 satisfies this, so the zigzag and stripe domains and the Néel and ferromagnetic wave vectors are available on each of them. The 24-site cluster is in addition C_3-symmetric and contains the K points, and the 32-site (4×4) cluster is C_3-symmetric but lacks K. The 48-site (6×4) cluster has neither, and the 72-site (6×6) cluster is again C_3-symmetric and contains the K points. The 2NN and 3NN bonds and the 2NN DM vectors are assigned by the same rules as on the ED cluster, with every periodic image counted once.

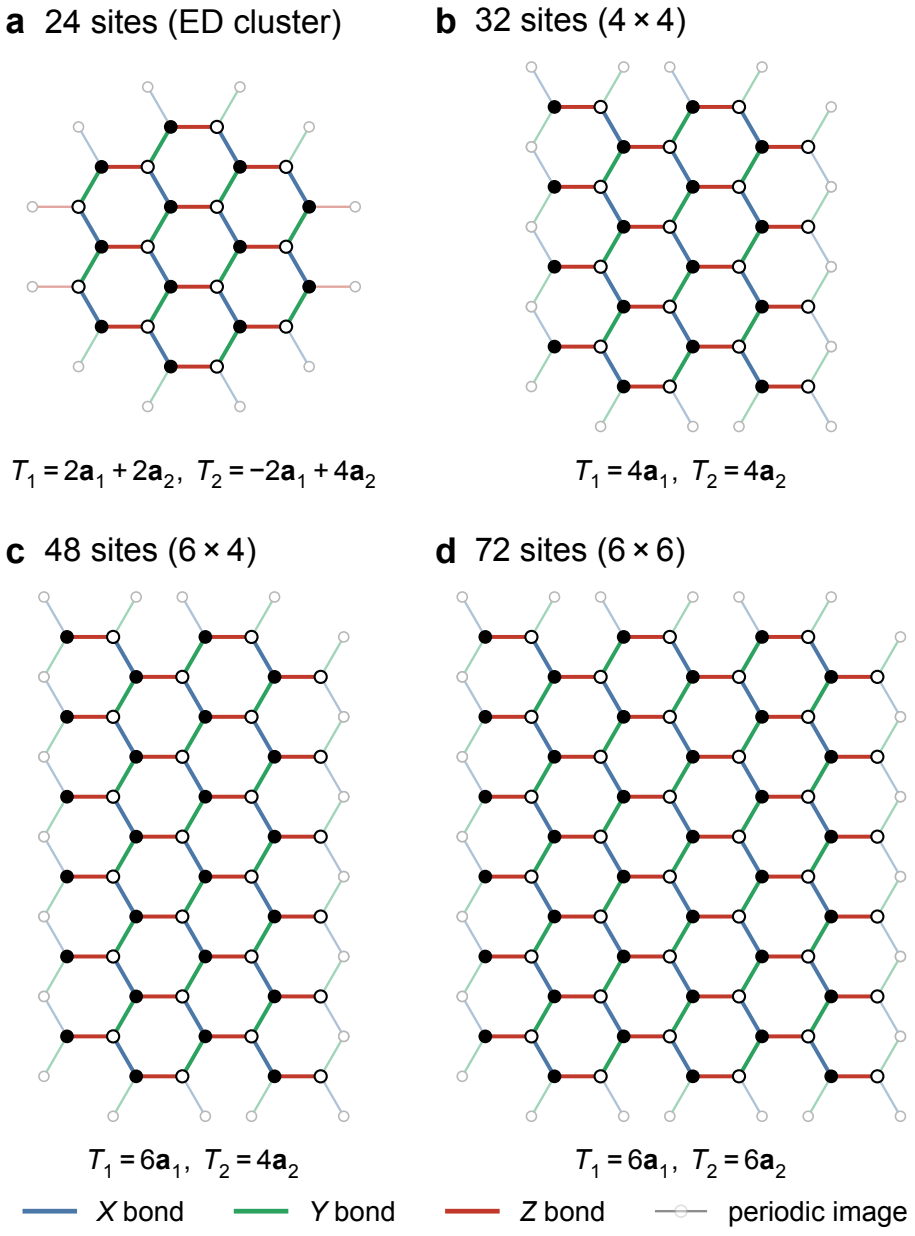

Figure S17. Periodic clusters of the DMRG calculations, drawn as in Fig. S9(d): (a) the 24-site cluster of the ED, (b) 32 sites (4×4), (c) 48 sites (6×4) and (d) 72 sites (6×6). The supercell vectors are given under each cluster.

We use the two-site DMRG [7] of ITensors [8] without conserved quantum numbers. The Hamiltonian is built as a matrix-product operator from bond tensors generated by a separate code, with the sites ordered along the supercell. The bond-dimension ladder is $\chi = 128$, 256, 512, 1000, 1500, 2000 with six to eight sweeps per stage and a discarded-weight cutoff of 10^{-10}. The maximum bond dimension depends on cluster size. The 24- and 32-site checks use random and zigzag-product initial states. The 32-site $\chi = 2000$ entry is available for the random initial state only. On 48 and 72 sites the bond-dimension series of Table S4 uses the random initial state. The pattern weights m_P^2 are those of Sec. IX. The solver reproduces a dense diagonalization of an 8-site cluster to 10^{-12}. On the 24-site cluster at the RuI_3 point, the DMRG energy converges from above onto the ED value. It reaches -94.587 meV at $\chi = 2000$ against the ED value of -94.589 meV, with the same order parameters ($m_N^2 = 0.097$ and 0.096 for each zigzag domain). Table S4 lists the results at the RuI_3 point. At the largest bond dimension tested with both initial states, their energies agree within 10^{-10} meV on 24 sites ($\chi = 2000$) and 3×10^{-4} meV on 32 sites ($\chi = 1000$). The summed weight of the three zigzag domains exceeds the Néel weight, and from 24 to 32 sites the Néel weight decreases from 0.097 to 0.070 while the summed zigzag weight stays at 0.27–0.29. On 32 sites, the energy per site still changes by 0.013 meV between $\chi = 1000$ and 2000, where 2000 is the largest bond dimension reached on this cluster. The three zigzag weights differ by at most 0.002 at $\chi = 2000$. Thus, the 32-site entries indicate a size trend but are not fully converged. The truncation errors of Table S4 are set by the bond-dimension cap, not by the cutoff.

Table S4. DMRG results for the RuI_3 couplings of Table 1 of the main text on the periodic clusters of Fig. S17: bond dimension χ, energy per site, truncation error of the last sweep, and the pattern weights m_P^2 of the ferromagnetic and Néel patterns and of the three zigzag domains.

N	χ	E/N (meV)	trunc. error	m_{FM}^2	m_{N}^2	m_{zz}^2 (X, Y, Z domains)
24	1000	−3.9394	2.6×10^{-4}	0.009	0.096	0.096, 0.096, 0.096
24	2000	−3.9411	3.0×10^{-5}	0.009	0.097	0.096, 0.096, 0.096
32	512	−3.8306	1.4×10^{-4}	0.008	0.052	0.035, 0.211, 0.035
32	1000	−3.8430	3.9×10^{-4}	0.008	0.065	0.086, 0.102, 0.083
32	2000	−3.8558	2.8×10^{-4}	0.008	0.070	0.088, 0.090, 0.088
48	512	−3.8090	2.8×10^{-5}	0.006	0.031	0.021, 0.217, 0.021
48	1000	−3.8124	1.6×10^{-5}	0.006	0.032	0.022, 0.214, 0.022
48	1500	−3.8135	1.1×10^{-5}	0.006	0.033	0.022, 0.214, 0.022
72	256	−3.7639	5.1×10^{-5}	0.004	0.017	0.013, 0.225, 0.013
72	512	−3.7786	3.9×10^{-5}	0.004	0.018	0.013, 0.221, 0.013
72	1000	−3.7883	2.9×10^{-5}	0.004	0.019	0.014, 0.219, 0.014

On 48 sites the DMRG state selects one zigzag domain. At $\chi = 1500$ the truncation error is 1×10^{-5}, and the pattern weights recomputed from the saved correlation matrices are $m_N^2 = 0.0326$ and $m_{zz}^2 = 0.0220$, 0.2136 and 0.0220. The zigzag sum is 0.2577. The same quantities are 0.0311 and 0.2595 at $\chi = 512$ and 0.0321 and 0.2583 at $\chi = 1000$, so the bond dimension moves them by less than 0.002. The lack of C_3 symmetry makes the three zigzag domains inequivalent on this cluster.

The C_3-symmetric 72-site cluster also selects a single zigzag domain [Fig. S18]. At $\chi = 1000$ its weights are $m_N^2 = 0.0188$ and $m_{zz}^2 = 0.0135$, 0.2188 and 0.0135, with a zigzag sum of 0.2458. At $\chi = 512$ they are 0.0178 and 0.2476. The Néel weights thus decrease from 0.097 to 0.070, 0.033 and 0.019 across the four sizes. The summed zigzag weights remain substantial but decrease slightly, from 0.288 to 0.266, 0.258 and 0.246. This trend supports stronger relative zigzag character, not growth of the total zigzag weight.

The mean local pseudospin is 0.440 on 48 sites and 0.455 on 72 sites, and both are tilted by approximately 16.2° from c. The magnitudes vary from 0.439 to 0.440 on 48 sites and from 0.450 to 0.461 on 72 sites. The nonzero local pseudospins and the single domain arise because the DMRG state at finite bond dimension breaks the symmetry, whereas the exact ground state of a finite cluster is symmetric. The 72-site structure factor is shown in Fig. 6(d) of the main text. Its peak-to-average ratio is 17.5, compared with 11.4 on 48 sites. These ratios depend on system size and domain selection.

Pinning fields provide a complementary comparison of responses to the Néel and zigzag patterns. We add $-h \sum_i \epsilon_i^P \, \mathbf{n}_P \cdot \mathbf{S}_i$ to the Hamiltonian, where $\epsilon_i^P = \pm 1$ are the signs of the pattern and $\mathbf{n}_P$ is its easy axis from Sec. XI. This term is the periodic-cluster version of the pinning fields used in DMRG studies of magnetic order [9, 10]. We record the induced order parameter $m_P(h) = N^{-1} \sum_i \epsilon_i^P \, \mathbf{n}_P \cdot \langle \mathbf{S}_i \rangle$ at $\chi = 1000$ (Table S5). On 48 sites, the zigzag field is applied to the domain that the cluster selects. On 24 and 32 sites the Néel response is linear with a slope m_N/h of 0.6–0.7 meV^{-1}, and it decreases to 0.26 meV^{-1} on 48 sites. The zigzag response instead grows from a slope

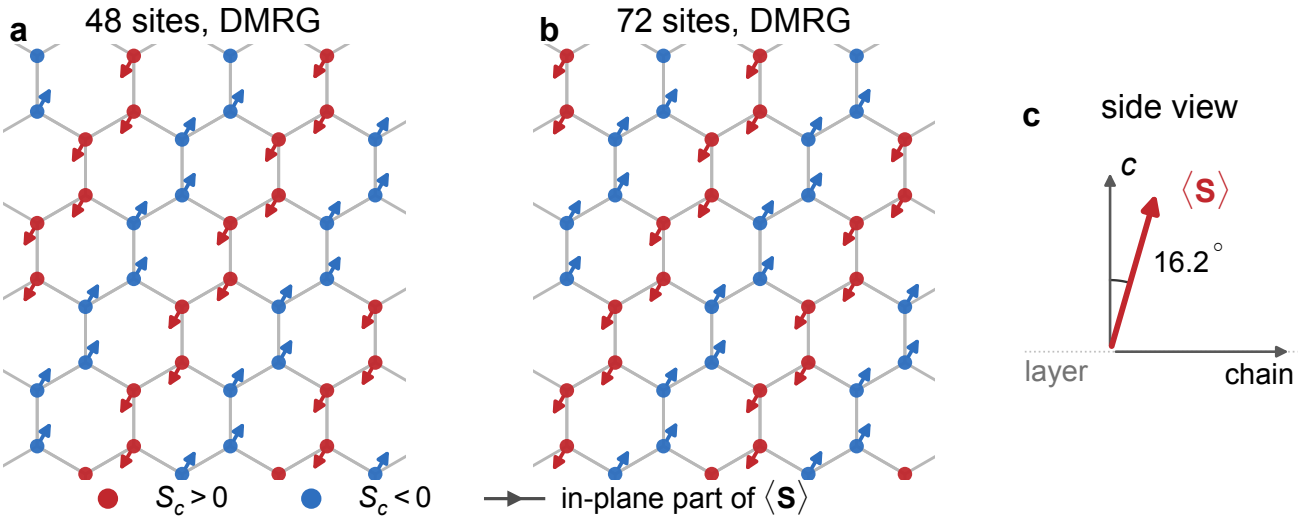

Figure S18. DMRG ground states of the 48-site ($\chi = 1500$) and 72-site ($\chi = 1000$) clusters for the RuI_3 couplings. (a),(b) Top view along c. Arrows show the in-plane part of each local pseudospin $\langle \mathbf{S}_i \rangle$, and the disc color shows its c component. A full pseudospin of 1/2 would be drawn as 1.5 bond lengths. (c) Side view in the plane of c and the chain direction.

of 1.4 meV^{-1} on 24 sites to $m_{zz} = 0.37$ of the maximum 0.5 at $h = 0.05$ meV on 32 sites and to 0.44 on 48 sites, which is 88% of saturation. Doubling the field on 48 sites changes it by less than 0.002. The Néel response therefore decreases with the cluster size while the zigzag response grows towards saturation.

Table S5. Response to a pinning field $-h \sum_i \epsilon_i^P \, \mathbf{n}_P \cdot \mathbf{S}_i$ for the RuI_3 couplings: induced order parameter $m_P(h)$ (maximum 0.5) of the Néel and zigzag patterns from DMRG at $\chi = 1000$.

N	h (meV)	m_{N}	m_{zz}
24	0.05	0.030	0.072
24	0.1	0.060	0.147
24	0.2	0.116	0.281
32	0.05	0.034	0.374
32	0.1	0.071	0.413
48	0.05	0.013	0.442
48	0.1	0.026	0.443

Figure S19 repeats the full scan of Fig. 5(c) of the main text with DMRG at $\chi = 512$ on 101 of the 201 points, analyzed in the same way as the ED data. The ground-state energy, its curvature and the order parameters m_P^2 of the ferromagnetic, Néel, zigzag and stripe patterns follow the ED curves point by point. For zigzag and stripe, this holds for each of the three domains. The energy lies above the exact value by at most 0.23 meV (0.25%, in the crossover region around RuI_3) and by 0.003 meV in the ordered regions. The order parameters agree within 0.003 and the spin correlations to better than 0.01. The phase bar built from the DMRG data reproduces that of the ED panel: the curvature peaks fall at 0.76π and 1.48π in both, every edge of the phase bar agrees to 0.005π, and $b = 0.21$ at the RuI_3 point in both.

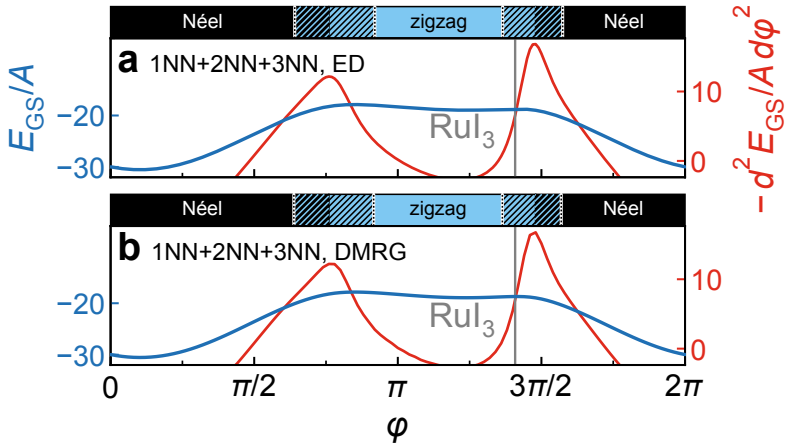

Figure S19. ED and DMRG with the 1NN, 2NN and 3NN couplings on the 24-site cluster, drawn as Fig. 5(c) of the main text: (a) ED at 201 points and (b) DMRG at $\chi = 512$ at 101 points. The phase bar of (b) is built from the DMRG data alone.

XI. Linear spin-wave theory

The Néel and zigzag states compete on the 24-site cluster. Linear spin-wave theory tests at the harmonic level whether both are stable ordered states of the infinite lattice. For each site of a collinear state, we choose a local orthonormal frame $(\mathbf{e}_{1i}, \mathbf{e}_{2i}, \mathbf{n}_i)$, where $\mathbf{n}_i = \pm\mathbf{n}$. The Holstein–Primakoff expansion is $\mathbf{S}_i = S\mathbf{n}_i + \sqrt{S/2}\,(\mathbf{u}_i a_i + \mathbf{u}_i^* a_i^\dagger) - \mathbf{n}_i a_i^\dagger a_i$, with $\mathbf{u}_i = \mathbf{e}_{1i} - i\mathbf{e}_{2i}$. We substitute this expression into $\sum_{\langle ij\rangle} \mathbf{S}_i^T \mathsf{J}_{ij} \mathbf{S}_j$ with the 2NN DM interaction included and keep the quadratic terms. Each bond is counted once. With $S = 1/2$ and the magnetic cell of the state (two sites for Néel and four for zigzag), the quadratic Hamiltonian without its constant term is

$$H_2 = \frac{1}{2}\sum_{\mathbf{k}} \Psi_{\mathbf{k}}^\dagger \mathsf{H}(\mathbf{k}) \Psi_{\mathbf{k}}, \qquad \mathsf{H}(\mathbf{k}) = \begin{pmatrix} \mathsf{A}(\mathbf{k}) & \mathsf{B}(\mathbf{k}) \\ \mathsf{B}^\dagger(\mathbf{k}) & \mathsf{A}^*(-\mathbf{k}) \end{pmatrix}, \tag{S4}$$

with $\Psi_{\mathbf{k}} = (a_{1\mathbf{k}}, \ldots, a_{1,-\mathbf{k}}^\dagger, \ldots)$. The linear terms vanish because both states are stationary points of the classical energy, which we verified to 10^{-9} meV. A positive-definite $\mathsf{H}(\mathbf{k})$ gives real magnon frequencies $\omega_n(\mathbf{k})$. Zero modes require separate treatment of a positive-semidefinite matrix. We test local classical stability with the smallest eigenvalue $\lambda_{\min}(\mathbf{k})$ of $\mathsf{H}(\mathbf{k})$. A negative value means that a transverse modulation at wave vector $\mathbf{k}$ lowers the classical energy. For a stable state the zero-point correction is $\Delta E_0 = \frac{1}{2}\sum_{\mathbf{k}} \big[\sum_n \omega_n(\mathbf{k}) - \operatorname{tr} \mathsf{A}(\mathbf{k})\big]$, and the harmonic energy is $E_{\rm cl} + \Delta E_0$. The implementation reproduces the honeycomb Heisenberg ferromagnet (zero-point correction below 10^{-12}) and the closed-form value for the antiferromagnet ($\Delta E_0 = \frac{3}{2} JS\,[\langle\sqrt{1-|\gamma_{\mathbf{k}}|^2}\rangle - 1] = -0.15738\,J$ per site). In addition, ΔE_0 of the zigzag state is invariant under a refolding of the magnetic cell from 2×2 to 4×2 unit cells (-0.41443 meV per site on both).

Figure S20 shows the result for the six-site couplings of Table 1 of the main text. For zigzag, the moment lies along the classical easy axis of the domain of Fig. S18. With this moment direction, $\lambda_{\min}(\mathbf{k}) \geq 2.3$ meV over the whole zone, and the four magnon branches are real everywhere and span 6.7 to 15.9 meV. The gap of 6.7 meV at Γ is the anisotropy gap of a state that breaks only discrete symmetries. The zero-point correction is -0.414 meV per site on top of the classical -3.328 meV. For the Néel orientation shown, the moment lies in the classical easy plane parallel to the honeycomb layer. For this state, $\lambda_{\min}(\mathbf{k})$ is negative over one quarter of the zone in pockets around the M points, with -2.2 meV at M and -1.7 meV at 0.83 of the way from Γ to M. It reaches about $+8$ meV near K on the sampled grid. The zero at Γ is a harmonic mode associated with the accidental classical easy-plane degeneracy. Along Γ–M–K–Γ [Fig. S20(d)], the lowest Néel branch becomes imaginary over one quarter of the path, with $|\mathrm{Im}\,\omega|$ up to 6.2 meV. Thus, the Néel state is not a local minimum of the classical energy, and it relaxes along the wave vector of zigzag order itself. This instability is due to the ferromagnetic 1NN Kitaev coupling. Both states satisfy the antiferromagnetic J_3 equally, but Néel gains only -0.19 meV per site from the 1NN couplings against -1.38 meV for zigzag. The 2NN couplings and the anisotropic 3NN terms favor Néel by only 0.41 and 0.22 meV. Accordingly, switching off K_1 alone makes $\lambda_{\min}(\mathbf{k})$ non-negative everywhere [Fig. S20(b),(e)], whereas switching off Γ_1, Γ_1', the 2NN couplings, or J_3 makes $\lambda_{\min}$ more negative. The 24-site ED energy is -3.94 meV per site, 5% below the infinite-lattice harmonic zigzag value of -3.74 meV per site.

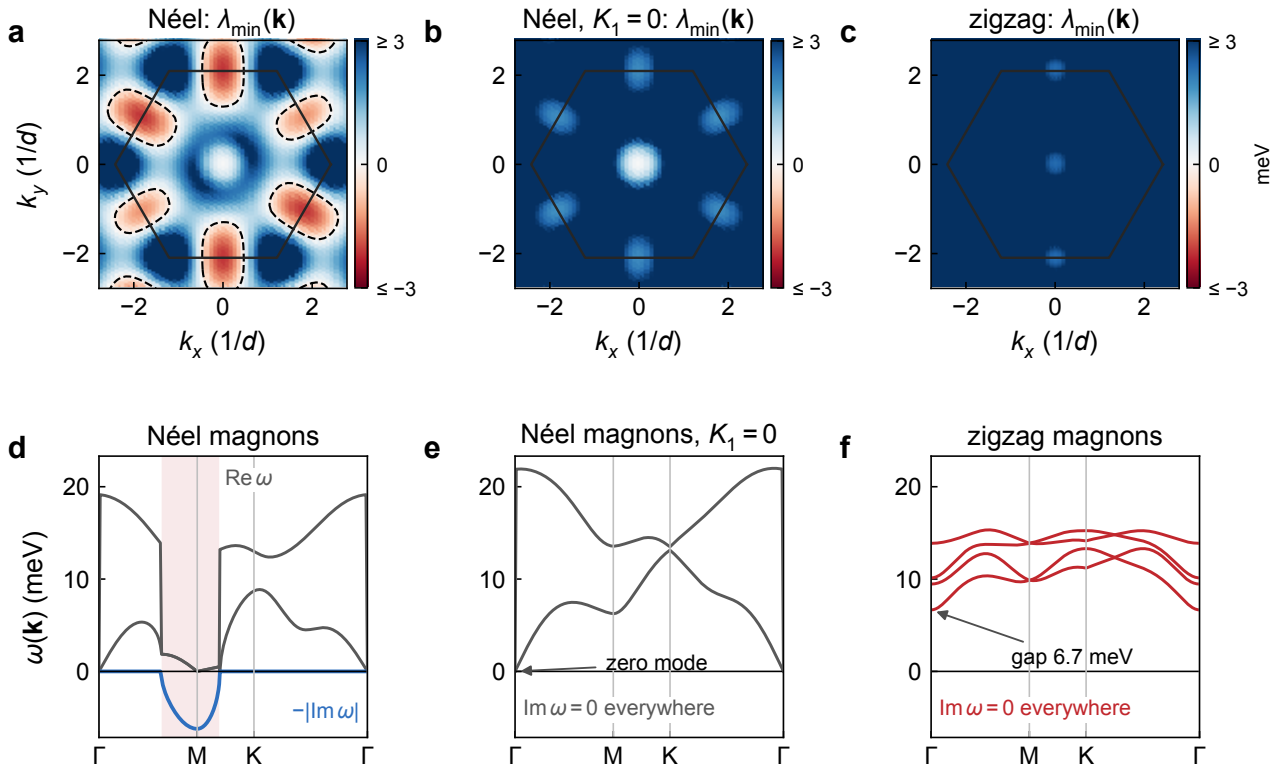

Figure S20. Linear spin-wave stability of the Néel and zigzag states with the 1NN, 2NN and 3NN couplings. Top row: smallest eigenvalue $\lambda_{\min}(\mathbf{k})$ of the harmonic Hamiltonian $\mathsf{H}(\mathbf{k})$ of Eq. (S4) over the Brillouin zone for (a) Néel with the moment in the easy plane, (b) the same state with K_1 set to zero and (c) zigzag with the moment along its easy axis. The hexagon is the first zone, and d is the Ru–Ru distance. The color scale is saturated at ± 3 meV, and the dashed contour marks $\lambda_{\min} = -0.15$ meV. Bottom row: Bogoliubov spectra along Γ–M–K–Γ for (d) Néel, (e) Néel with $K_1 = 0$ and (f) zigzag. In (d), the imaginary part is plotted downward in blue and the unstable region is shaded.

XII. Monte Carlo simulations

We study the finite-temperature ordering by Monte Carlo (MC) simulations with the pseudospins treated as classical vectors of length $|\mathbf{S}| = 1/2$ on periodic $L \times L \times 2$ honeycomb clusters, with $L = 8$, 12, 16 and 24. Metropolis sweeps are followed by overrelaxation updates. Each run uses 3000 equilibration and 9000 measurement sweeps at each of 60 geometrically spaced temperatures from 60 to 2 K. We use three independent random seeds per size. The proposal width of the Metropolis step is adjusted during equilibration and held fixed during measurement. The grid spacing is about 1 K near 18 K and 0.7 K near 12 K. We locate the specific-heat maximum after three-point smoothing of $C_v(T)$. The grid sets the temperature resolution. As seen in Fig. S21(a),(c), the pseudospin Hamiltonian with only the six-site 1NN couplings of Table 1 of the main text orders ferromagnetically at $T_c \approx 18$ K for every L. Its ground state is collinear, with a moment of $1.20\,\mu_B$ along c for $g_c = 2.40$.

With the six-site 2NN and 3NN couplings of Table 1 of the main text added [Fig. S21(b),(d)], the seed-averaged specific heat peaks at 12.65 K for $L = 8$ and 11.94 K for $L = 12$, 16 and 24. The two values differ by one temperature-grid step. For $L = 8$, the inset instead shows the mean of the three individual peak temperatures, which is 12.42 K with a standard deviation of 0.33 K. The low-temperature zigzag order parameter approaches saturation, while the ferromagnetic and Néel parameters are below 0.02 at 2 K. In these simulations the zigzag state lies 0.58 meV per site below the Néel state.

Every run ends with a zero-temperature relaxation of its lowest-temperature configuration, and the relaxed structures are shown in Fig. S22. Both relaxed states are collinear, with $|\mathbf{S}| = 1/2$ on every site. At 2 K, the mean spin projection onto the relaxed pattern reaches 97%–98% of saturation. With only the 1NN couplings the moment points along c. With the 2NN and 3NN couplings the state is zigzag, with ferromagnetic chains of X and Y bonds antiparallel across the Z bonds. The pseudospin is tilted by 17.7° from c toward the chain direction and points along

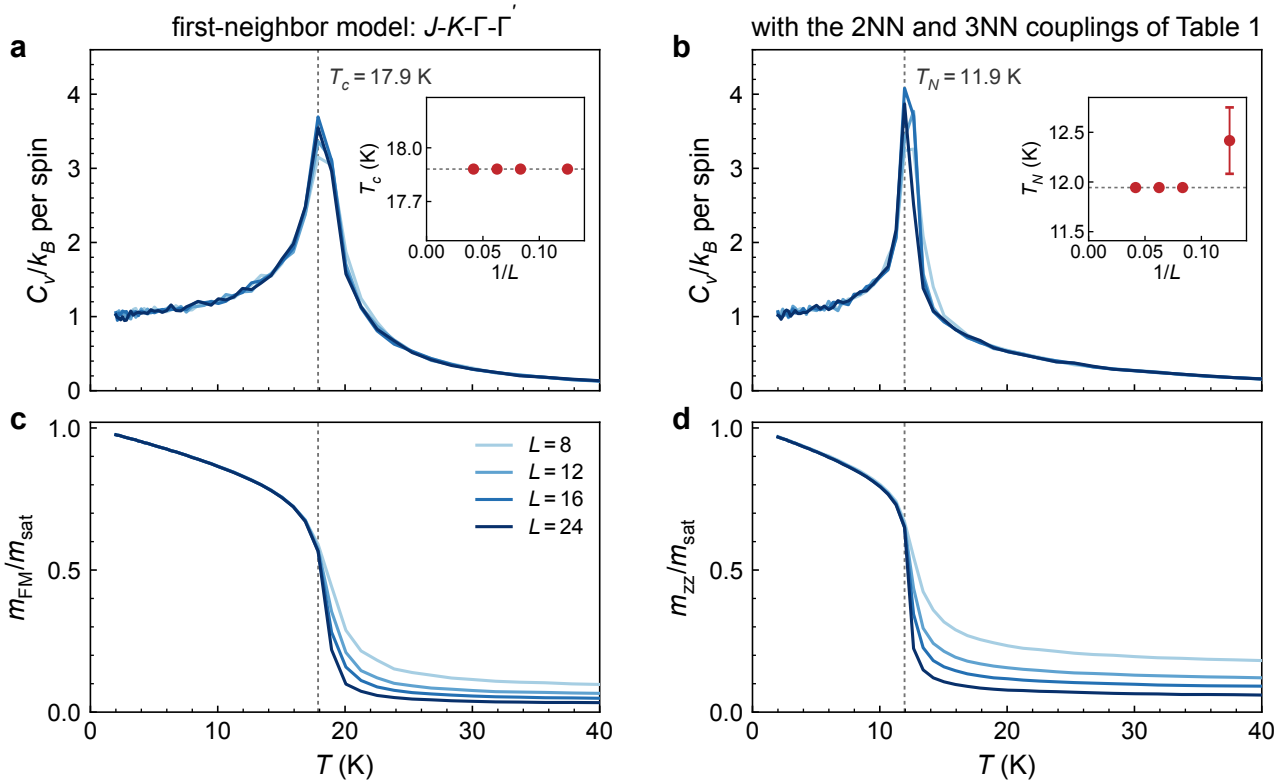

Figure S21. Monte Carlo simulations of the RuI_3 pseudospin model on $L \times L \times 2$ honeycomb clusters with $L = 8$, 12, 16 and 24: (a),(c) only the 1NN couplings of Table 1 of the main text and (b),(d) the 1NN, 2NN and 3NN couplings. The top row shows the specific heat per spin and the bottom row the order parameter normalized to its saturation value. The dotted line marks the $L = 24$ peak temperature. The insets show the mean peak temperature of three seeds against $1/L$, with one standard deviation as the error bar.

(0.674, 0.674, 0.302) in cubic axes. For the magnetic moment $\mathbf{M} = \mu_B(g_{ab}S_{ab}, g_cS_c)$ with $g_c = 2.40$ and $g_{ab} = 1.79$ the tilt is 13.4°. The three seeds sample the three C_3-related zigzag domains. Their ferromagnetic chains use the two bond types complementary to the antiferromagnetic bond type. The anisotropy tensor of the zigzag pattern has three non-degenerate eigenvalues of −3.33, −2.02 and −0.67 meV per site, so the ordered state breaks only discrete symmetries. The weak low-temperature size dependence in Fig. S21 is consistent with this anisotropic ordered state.

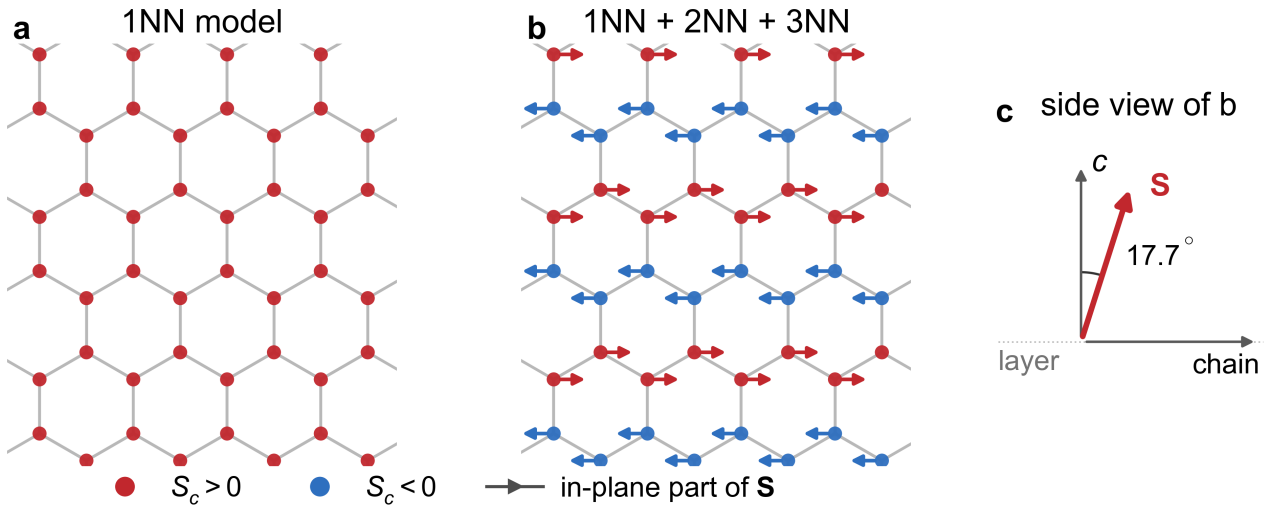

Figure S22. Zero-temperature spin configurations of the two sets of couplings of Fig. S21 from the relaxed $L = 24$ runs. Each arrow represents the spin of one site. (a),(b) Top view along c for (a) only the 1NN couplings and (b) the 1NN, 2NN and 3NN couplings. The view is rotated by 90° with respect to Fig. 1 of the main text so that the Z bond is vertical. The disc color gives the sign of the c component, and the arrow gives the in-plane part. (c) Side view of (b) in the plane of c and the chain direction.

[1] Gretarsson, H. *et al.* $J = 1/2$ pseudospins and *d-p* hybridization in the Kitaev spin liquid candidates RuX_3 (X = Cl, Br, I). *Phys. Rev. B* **109**, L180413 (2024).

[2] Liu, L. *et al.* Contrasting electronic states of RuI_3 and $RuCl_3$. *Phys. Rev. B* **107**, 165134 (2023).

[3] Mostofi, A. A. *et al.* wannier90: a tool for obtaining maximally-localised Wannier functions. *Comput. Phys. Commun.* **178**, 685–699 (2008).

[4] Winter, S. M., Li, Y., Jeschke, H. O. & Valentí, R. Challenges in design of Kitaev materials: magnetic interactions from competing energy scales. *Phys. Rev. B* **93**, 214431 (2016).

[5] Kitaev, A. Anyons in an exactly solved model and beyond. *Ann. Phys.* **321**, 2–111 (2006).

[6] Baskaran, G., Mandal, S. & Shankar, R. Exact results for spin dynamics and fractionalization in the Kitaev model. *Phys. Rev. Lett.* **98**, 247201 (2007).

[7] White, S. R. Density matrix formulation for quantum renormalization groups. *Phys. Rev. Lett.* **69**, 2863–2866 (1992).

[8] Fishman, M., White, S. R. & Stoudenmire, E. M. The ITensor software library for tensor network calculations. *SciPost Phys. Codebases* 4 (2022).

[9] White, S. R. & Chernyshev, A. L. Néel order in square and triangular lattice Heisenberg models. *Phys. Rev. Lett.* **99**, 127004 (2007).

[10] Stoudenmire, E. M. & White, S. R. Studying two-dimensional systems with the density matrix renormalization group. *Annu. Rev. Condens. Matter Phys.* **3**, 111–128 (2012).